INVITED PAPER

Theory, Analysis, and Design of Metasurfaces for Smart Radio Environments

This article provides an overview of the fundamental theory behind reconfigurable intelligent surfaces, with focus on surface-wave and nonspecular reconfigurable reflective surfaces.

By E. MARTINI, *Senior Member IEEE*, AND S. MACI, *Fellow IEEE*

ABSTRACT | The term "metasurface" (MTS) denotes an artificial surface constituted by a distribution of electrically small elements that collectively exhibit equivalent homogeneous boundary conditions (BCs) to an interacting electromagnetic field. MTSs are becoming increasingly popular due to the technological simplification that they offer with respect to volumetric metamaterials. In this article, we review the basic theory behind microwave MTSs seen as reconfigurable intelligent surfaces (RISs), oriented to the future visionary challenge of a smart radio environment. To this end, two different typologies of MTS are reviewed: surface-wave-based MTSs and nonspecular reflective MTSs. Both types can be effectively characterized using simplified problems that locally match the homogenized, modulated BCs. A different use of these problems allows for an accurate design of radiated and scattered fields. An accurate ray representation is also suggested, which allows for an effective description of the scattered field also in the Fresnel region and for the insertion of the MTS description in ray-tracing tools for network planning. Several examples of practical implementation are shown, and the challenges in applying electronic reconfigurability are discussed.

KEYWORDS | Fifth generation (5G); metasurfaces; reflective Intelligent surfaces; sixth generation (6G); smart radio environment (SRE); wireless communications.

Manuscript received 7 October 2021; revised 14 February 2022; accepted 17 April 2022. Date of publication 25 May 2022; date of current version 19 September 2022. This work was supported in part by the European Space Agency (ESA-ESTEC, The Netherlands) and in part by the Italian Ministry of the Research through a Project of Relevant Italian Interest (PRIN). The work of E. Martini was supported by the University of Siena through the funding of a Curiosity Driven (F-CUR) project in the framework of the program Piano di Sostegno alla Ricerca (PSR) 2021. *(Corresponding author: S. Maci.)*
The authors are with the Department of Information Engineering and Mathematics, Università di Siena, 53100 Siena, Italy (e-mail: martini@dii.unisi.it; macis@dii.unisi.it).

Digital Object Identifier 10.1109/JPROC.2022.3171921

I. INTRODUCTION

The last years have experienced a continuous growing request for massive and ubiquitous multimedia information access. Together with these impressive data rates, future wireless networks are expected to offer sensing, localization, low-latency, and ultrareliable communications. The fifth-generation (5G) network is currently faced with the challenge of limited data speed, exacerbated by the proliferation of billions of data-intensive applications. Radically new communication paradigms, especially at the physical layer, are required to handle this problem. In this context, the revolutionary concept of a smart radio environment (SRE) has recently emerged as a new paradigm for wireless communications, in which the environment is controlled and programed jointly with the transmitters and receivers, rather than something to compensate for.

The sixth generation (6G) needs a new architectural platform not only for transmission/reception but also for sensing, communication, computing, and, above all, an environment that can be cooperative and programmable; this visionary concept is denoted as SRE. The key technology underpinning SREs is represented by metasurfaces (MTSs) of next generation, which can be denoted with the general acronym of reconfigurable intelligent surfaces (RISs) [1]–[5]. MTS-based RISs consist of electrically small elements whose electromagnetic (EM) behavior is electronically controlled to properly tailor the macroscopic EM behavior. MTSs do not require signal processing nor signal amplification, so they have extremely low power consumption, and they can process EM signals directly at the speed of light, dramatically reducing latency and complexity with respect to the corresponding fully digital solutions. Hence, an RIS can be thought of as an inexpensive adaptive (smart) skin, which covers parts of walls,

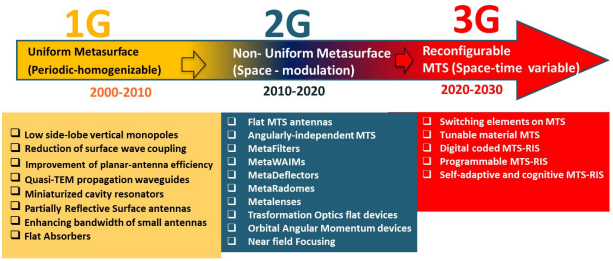

Fig. 1. *Three generations of MTSs since 2000 and relevant applications in antenna and microwaves.*

buildings, and ceilings, and can modify and control the radio waves' paths, and sense the environment. A prominent property of RISs is, therefore, the capability of being reconfigured after their deployment.

MTSs have had and are having a strong impact on antenna and microwave applications [6]–[9]. In the years 2000–2010, MTSs were essentially uniform in space and realized by periodic arrangements of printed elements. This was the first generation of MTSs. Several new applications in microwaves and antennas were born in that period; examples are those listed in Fig. 1. In the second generation (2010–2020), MTSs were designed in such a way to change boundary conditions (BCs) in space to control the field launched by an in-plane or external feed. Today, leveraging on the developments of the second generation, we are facing a transition to a third generation, where MTSs change BCs in space and time, becoming controllable and intelligent. MTS reconfigurability can be achieved by using electronics, time-changing materials, or multiple switchable feed points distributed over the MTS. The possibility to independently control the individual elements gave rise to the concept of "digital-coding MTSs" [10], [11], which evolved into "programmable MTSs" after introducing a field-programmable gate array to control different MTS functionalities based on different digital states of the elements [12], [13]. This concept can be further extended to self-adaptive and cognitive MTSs [15].

Reconfigurability makes the MTS amenable to a massive MIMO and capable to reroute signals in nonspecular directions. Therefore, reconfigurable MTSs become a key enabling technology for the future generation of sensing and communications, as the basic constituent of a fully intelligent and cooperative wireless environment.

We should remark that an RIS can be also realized with the well-established technology of reflectarrays [17]. Reflectarrays differ from MTSs essentially because the printed scatterers are resonant and, therefore, comparable with half the characteristic wavelength of the substrate where they are printed. In MTSs, the elements are small with respect to this wavelength, and therefore, they can be globally modeled as a continuous impedance boundary. This simple difference makes MTSs more capable than reflectarrays in manipulating the EM field even though more challenging to be reconfigured at a low cost due to the complexity of the control network.

In this article, we will review models, design, analysis, and synthesis tools for MTSs and present several examples of RIS and surface-wave-based antennas/sensors. The perspective of the third generation of MTSs is discussed with an emphasis on the performance, speed, losses of the various configurations, and applicability in beyond 5G scenarios.

II. SPACE WAVE VERSUS SURFACE WAVE INTERACTION WITH MTS

MTSs can be categorized depending on the different interaction mechanisms between the wave and the MTS, and can be designed for three different purposes, as illustrated in Fig. 2: to achieve unusual reflection/transmission properties of space waves [18]–[22], to modify the dispersion properties of surface/guided waves [23]–[25], or to operate a conversion between a surface wave (SW) and a space wave (or vice versa) [26]–[29].

The first category is sometimes denoted as gradient MTS and can serve for realizing nonspecular reflective surfaces [see Fig. 2(a)] or metadeflectors [see Fig. 2(b)]. In this type of MTS, the output beam can be readdressed by changing the linear phase introduced by the MTS while maintaining low levels of specular reflection or direct transmission contributions. The cases illustrated in Fig. 2(c) and (d) are denoted as MTS lenses since they

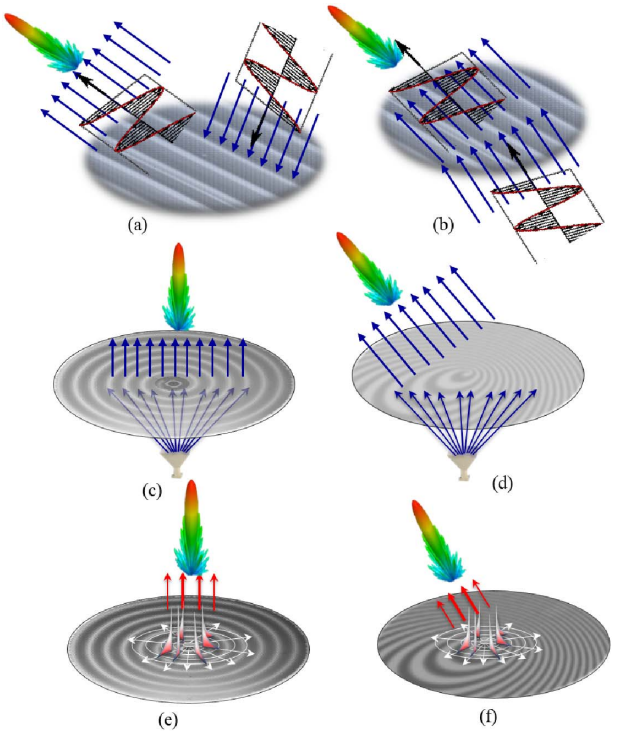

Fig. 2. *Different types of MTS-based RIS. (a) and (b) Phase gradient RIS. (a) Nonspecular reflective surface. (b) MTS deflector. Metalenses with (c) broadside and (d) tilted beam and relevant impedance holographies. (e) and (f) Surface-wave-based MTS with (e) broadside and (f) tilted beam.*

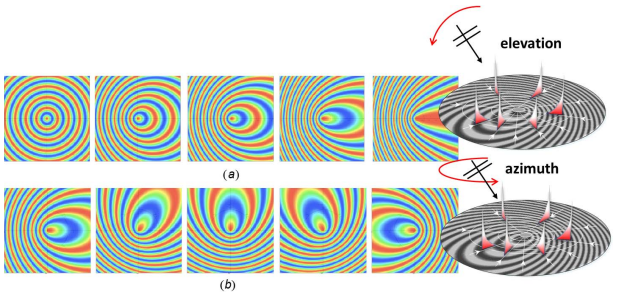

Fig. 3. *Layout of the impedance modulation for an MTS sensor, which allows for SW coupling in receiving mode. Variation of the (a) elevation angle and (b) azimuth angle.*

perform the same function as optical lenses. The modulation of the MTS impedance changes from cylindrical to elliptical. The cases in Fig. 2(e) and (f) represent SW-based antennas, where the feed is an in-plane monopole and the exciting wave is an SW with a cylindrical wavefront. The challenging problem in cases (a)–(d) is the cancellation of the specular reflections or direct transmission; in (e) and (f), the difficulty is, instead, the effective excitation of the SW, along with the control of the leakage attenuation constant along the SW path. Indeed, the periodic modulation of the BCs transforms the SW launched by the feed into a curvilinear wavefront leaky wave (LW), thus generating a radiating aperture with an amplitude control obtained through a proper design of the 2-D distribution of the attenuation constant. This results in a lightweight and low-profile structure, characterized by low losses and simple low-cost manufacturing. Furthermore, by acting on the BCs pattern, it is possible to obtain a unique control also of the phase and polarization of the aperture field, thus molding the radiation pattern.

We note that all the above configurations, and not only (a) and (b), can be of use in SREs. In fact, configurations (c) and (d) can be used as relay and (e) and (f) for sensing the environment. In particular, the SW-based MTS in receiving mode [i.e., the reciprocal configuration of Fig. 2(e) and (f)] can detect the direction of arrival of a signal, as shown in Fig. 3. A variation of the BCs can generate a different coupling with an inward traveling SW with different amounts of power received at the port. The direction of arrival is detected when the maximum coupling to SW is obtained at the output port. This phenomenon is simple and extremely selective in angle for electrically large MTSs. The various colored maps in Fig. 3 give an idea of how MTS impedance modulation should change for maximizing the coupling with a plane wave coming from different elevation (a) and azimuth (b) angles.

III. METASURFACE MODELS AND CANONICAL PROBLEMS

The effective design of RIS devices requires the use of realistic models that are, at the same time, accurate enough to describe practical characteristics (losses, frequency dependency, MTS discretization, coupling among elements, and so on), sufficiently general to be applicable to different implementation technologies and adequately simple to allow for the analysis of electrically large structures. A key point should be the capability to embed the RIS EM description in propagation models for overall system performance estimates. The model based on the concept of equivalent impedance is well established for static MTSs and can be generalized to reconfigurable ones; it is presented in the following with an emphasis on the typologies (a), (e), and (f) in Fig. 2.

A. Equivalent Homogenized Boundary Conditions

Thanks to the subwavelength size of the constituent unit cells, MTSs can be conveniently described in terms of homogenized BCs of impedance type, relating the tangential components of the average electric and magnetic fields. This description allows one to disregard the electrically small details of the single elements, thus significantly reducing the computational burden and avoiding ill-conditioning problems in the numerical analysis.

For a modulated MTS, the definition of the effective BCs at each unit cell relies on a local periodicity assumption, i.e., it is derived by assuming the unit cell immersed in a *microperiodic* environment (see Fig. 4). With this terminology, we will refer to the subwavelength period of the small elements, in contrast with the macroperiod of the global modulation obtained by changing the printed element dimension (see Figs. 5 and 6).

For a generic MTS backed by a ground plane [see Fig. 4(b)], the BCs can be expressed in terms of an "impenetrable" equivalent tensor impedance $\underline{\underline{\mathbf{Z}}}$, which relates the average tangential electric and magnetic fields on the top interface of the MTS

$$\mathbf{E}_t\left(z=0^+\right)=\underline{\underline{\mathbf{Z}}}\cdot\hat{\mathbf{z}}\times\mathbf{H}_t\left(z=0^+\right). \tag{1}$$

From here on, bold characters will denote vectors, and bold characters underlined by double bars will indicate tensors. The tensor nature of the equivalent impedance accounts for the possible coupling between different polarizations. When the wavevector of the interacting wave lies in a

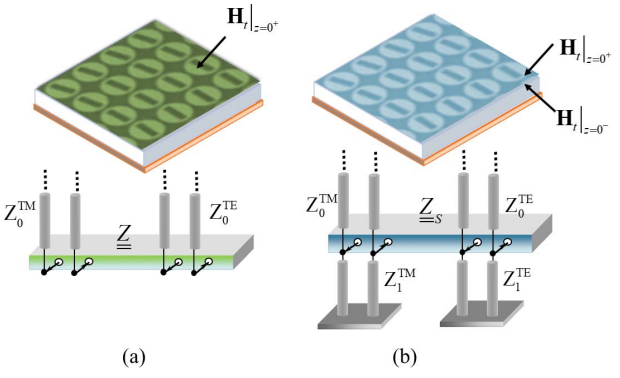

Fig. 4. *Geometry for the periodic MTS and corresponding equivalent transmission line model in homogenization assumption. (a) Opaque impedance model. (b) Penetrable impedance model.*

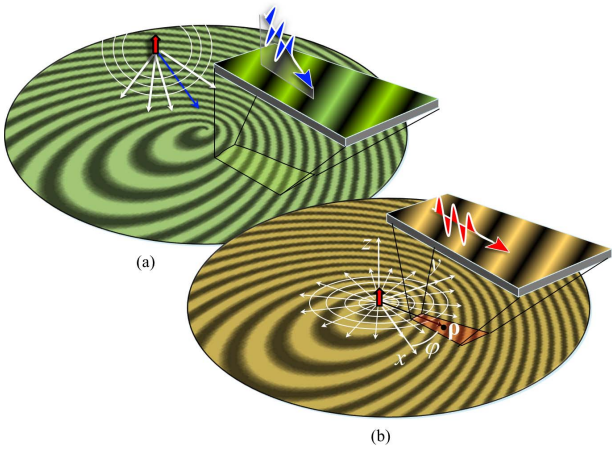

Fig. 5. *Local canonical macroperiodic homogenized problems for (a) space-wave illumination or (b) surface-wave illumination.*

symmetry plane of the MTS, there is no coupling, and scalar equivalent impedances equal to the eigenvalues of the tensors can be used for each polarization.

For static MTSs operating in the microwave and millimeter-wave ranges, losses can normally be neglected, and the equivalent impedance tensor $\underline{\underline{\mathbf{Z}}}$ is anti-Hermitian (namely, with purely reactive eigenvalues). For reconfigurable MTSs, however, losses are in general higher, and the tensor matrix loses the anti-Hermitian properties.

In the common case in which the MTS is realized by printing metallic patches on a grounded slab, a more accurate model can be defined relying on an equivalent transmission line description. According to this model, a *penetrable* impedance BC is introduced, which relates the tangential electric field to the discontinuity of the average tangential magnetic field across the metallization as follows:

$$\mathbf{E}_t\left(z=0\right)=\underline{\underline{\mathbf{Z}}}_s\,\hat{\mathbf{z}}\times\left[\mathbf{H}_t\left(z=0^+\right)-\mathbf{H}_t\left(z=0^-\right)\right]. \quad (2)$$

The relationship between $\underline{\underline{\mathbf{Z}}}$ and $\underline{\underline{\mathbf{Z}}}_s$ expressed in the TM/TE reference system of the interacting wave can be derived from the equivalent transmission line model as

$$\begin{bmatrix} Z^{ee} & Z^{eh} \\ Z^{he} & Z^{hh} \end{bmatrix}^{-1}=\begin{bmatrix} Z_s^{ee} & Z_s^{eh} \\ Z_s^{he} & Z_s^{hh} \end{bmatrix}^{-1}+\begin{bmatrix} Z_{sc}^{e} & 0 \\ 0 & Z_{sc}^{h} \end{bmatrix}^{-1} \quad (3)$$

where $Z_{sc}^{e/h}$ is the TM/TE reactance of the grounded slab. We note that $\underline{\underline{\mathbf{Z}}}_s$ possesses the same property of $\underline{\underline{\mathbf{Z}}}$ in the absence of losses.

The penetrable impedance model can be generalized to a generic multilayer environment and applied also to MTSs operating in transmission. In the presence of multiple printed layers, interlayer interactions can be accounted for by means of a multiport network based on the concept of "accessible modes" [30]. This model neglects ports associated with MTS-layer Floquet's modes that are sufficiently attenuated at contiguous layers.

Furthermore, it is noted that the penetrable impedance, which only represents the contribution of the patterned metallic layer, is only weakly dependent on the transverse wavenumber of the interacting field, as opposed to the impenetrable impedance, which models the whole finite thickness MTS. For this reason, the first model offers a significantly higher accuracy whenever the same BC has to be used for different wavenumbers [31], [32].

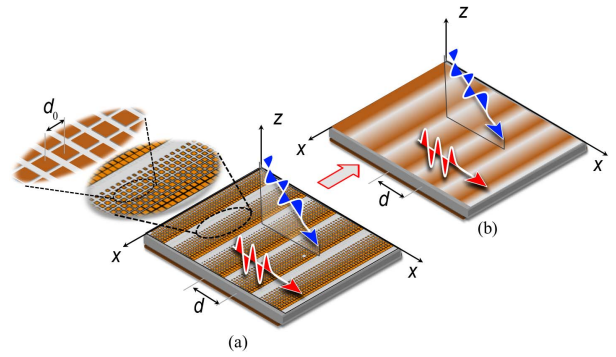

Fig. 6. *Geometry for (a) nonhomogenized and (b) homogenized canonical problems of a periodically modulated MTS with macroperiod d. In the inset on the right: printed elements and microperiod d_0 (red arrow denotes SW, and blue arrow denotes the homogeneous incident plane wave).*

B. Infinite Canonical Problem: Periodic Homogenized MTSs

Despite the apparent difference among them, various applications of spatially modulated MTSs share the same objective: tailoring the space spectrum of the excitation field, being it either a space wave or a surface wave. More specifically, two fundamental applications for SRE aim at generating fields with a wavenumber different from the one of the exciting wave. The first one is the case of anomalous reflection (case (a) in Fig. 2), where, given an incident space wave, we desire to generate a nonspecular reflected field while canceling the specular reflection. The second application is relevant to antennas and sensors based on SWs, where either the incident (cases (e) and (f) in Fig. 2) or the generated surface wave (see Fig. 3) propagates with phase velocity less than the speed of light. In both these cases, the objective is reached by introducing a (local) macroperiodicity in the homogenized MTS so that different space harmonics, or curvilinear-wavefront Floquet waves (FWs), can be generated. It is, therefore, important to formulate in a parametric way the analysis of the interaction of an EM plane wave with a periodically modulated unidirectional-gradient homogenized surface impedance, which matches the local BCs even in cases where the modulation is curvilinear (see Fig. 5).

This unidirectional-gradient, macroperiodic impedance problem represents, therefore, the "canonical" problem for the MTS design. (Note that we use here the term "canonical" even if the solution of the problem is not analytical

due to its numerically simple formulation and solution.) We stress again that we will refer to the periodicity of the impedance profile as a macroperiodicity d, as opposed to the microperiodicity d_0 related to the subwavelength unit cell used for the MTS implementation (see Fig. 6). An approach for a rigorous solution of the problem, which can be seen as a generalization of the approach proposed in [33], is described in the following.

Consider the geometry depicted in Fig. 6, where a periodically modulated MTS is excited by an EM plane wave field characterized by a transverse wavenumber k_{y0}. For the sake of simplicity, we will consider here a scalar impedance and a TM-polarized incident field, propagating along a direction orthogonal to the periodicity variation; however, the procedure illustrated here can be readily generalized to the case of tensor impedance, arbitrary polarization, and skew incidence [34].

This problem can be rigorously solved through a mode-matching method using FWs as modal functions. To this end, the Fourier series of the impedance profile and the FW expansion of the currents induced in the equivalent impedance surface are introduced

$$Z(y) = \sum_m Z_m e^{-j\frac{2\pi m}{d}y} \tag{4}$$

$$I(y)\hat{\mathbf{y}} = \hat{z} \times \mathbf{H}_t = \sum_n I_n e^{-jk_{yn}y}\hat{\mathbf{y}} \tag{5}$$

where k_{yn} are the FW wavenumbers given by

$$k_{yn} = k_{y0} + \frac{2\pi}{d}n \tag{6}$$

and d is the macroperiodicity. Notice that the currents in (5) may represent either the currents flowing in the metallic cladding or currents ideally flowing in an equivalent impenetrable impedance depending on the impedance model adopted.

The following step consists of the imposition of the BCs; the specific equations are slightly different depending on the type of problem, as illustrated in the following.

1) Scattering Problem: In a scattering problem, the transverse wavenumber k_{y0} is set by the incident field, and the objective is the control of the intensity of the FWs, at least the one falling in the visible region. After introducing Green's function to represent the scattered field, the equation imposing the BCs can be written as

$$\sum_{m,q} Z_m I_q e^{-j\frac{2\pi(m+q)}{d}y} = \sum_n G_{EJ}(k_{yn}) I_n e^{-j\frac{2\pi n}{d}y} + E_{y0}^{\text{inc}} \tag{7}$$

where a common dependency $\exp(-jk_{y0}y)$ has been suppressed, $G_{EJ}(.)$ is the spectral Green's function relating the electric current to the tangential electric field, and E_{y0}^{inc} is a constant representing the complex amplitude of the incident field. Both sides of (7) are periodic functions of the spatial coordinate y; therefore, they can be expanded in the Fourier series. After equating the corresponding coefficients of the series, for any n-index, we get

$$\sum_m I_m Z_{n-m} = G_{EJ}(k_{yn}) I_n + E_{y0}^{\text{inc}}\delta_{n,0} \tag{8}$$

where $\sum_m I_m Z_{n-m} = [\{\tilde{Z}\} \otimes \{\tilde{I}\}]_n$ is the nth term of the convolution between the impedance and current expansion coefficients, and $\delta_{i,j}$ is the Kronecker delta. For all n, (8) can be written in the form of an infinite linear system in the unknowns I_m

$$\sum_m \zeta_{n,m} I_m = E_{y0}^{\text{inc}}\delta_{n,0} \tag{9}$$

with

$$\zeta_{n,m} = Z_{n-m} - G_{EJ}(k_{yn})\,\delta_{n,m}. \tag{10}$$

In numerical evaluation, the Fourier expansions can be truncated to a finite number of terms (generally convergence is reached with few tens of terms). This leads to a finite linear system, whose solution provides the current coefficients I_m and, hence, the scattered fields.

Before proceeding further, we observe that the approach described here is very different from a localized physical optics (PO)-like approach, as the one used for reflectarray analysis [17] or in the so-called generalized reflection law [35]. The latter assumes that the field reflected at any point can be approximated with the one reflected by the infinite uniform surface, which locally approximates the modulated MTS [36], and therefore, it fails to correctly account for the macromodulation and the MTS spatial dispersion. The approach indicated here, instead, accounts for these effects, and therefore, it provides much more accurate results [37]. This aspect is quantitatively investigated in Section V.

2) SW-Coupling Model: When considering the SW-coupling model [see Fig. 5(b)], the objective is to find the modes supported by the periodic structure in transverse resonance conditions and control the relevant complex propagation constant. The problem is, therefore, formulated as an eigenvalue problem, where the transverse wavenumber k_{y0} is an unknown of the problem, and it is, in general, complex to account for the leakage of the -1 indexed (leaky)-mode. This represents the main difference with the scattering problem, where k_{y0} is imposed by the incident wave. The equation to be satisfied in the SW coupling is

$$\sum_{m,q} Z_m I_q e^{-j\frac{2\pi(m+q)}{d}y} = \sum_n G_{EJ}(k_{yn}) I_n e^{-j\frac{2\pi n}{d}y} \tag{11}$$

which, similar to what has been shown in Section III-B1, can be cast in the form of the following homogeneous linear system:

$$\sum_m \zeta_{n,m} I_m = 0 \tag{12}$$

where the matrix $\zeta_{n,m}$ is still given by (10). The complex wavenumber of the supported 0-indexed mode is then determined by setting to zero the determinant of the system matrix [32]. The relevant current distribution is given by the eigenvector corresponding to the zero eigenvalue. This is a fundamental piece of information, e.g., for studying field polarization in the case of anisotropic MTSs.

IV. MTS ANALYSIS

A. Scattering From a Finite Polygonal, Nonspecular Reflecting RIS

An MTS designed to redirect an impinging beam in one or more predefined directions will consist of a finite repetition of the macroperiods analyzed in Section III-B. The equivalent current distribution is, therefore, obtained by arranging the FW-based current modes over the aperture and formulating the radiation integral of it over the truncated structure.

For the sake of simplicity, we refer to a planar aperture with arbitrary polygonal contour, illuminated by a plane wave propagating in the direction

$$\hat{\mathbf{k}}_{inc} = \frac{1}{k}\left(k_{x0}\hat{x} + k_{y0}\hat{y} + \hat{\mathbf{z}}\sqrt{k^2 - k_{x0}^2 - k_{y0}^2}\right) \tag{13}$$

where k is the free space wavenumber, in which the electric currents are given by a superposition of plane waves coming from the solution of the problem in (9), with current amplitudes $I_{nm,x}$ and $I_{nm,y}$ along directions x and y, for the FW contributions with transverse-to-z wavenumbers

$$\begin{aligned}\mathbf{k}_{nm} &= k_{xn}\hat{x} + k_{ym}\hat{y} \\ &= \left(k_{x0} + \frac{2\pi}{d_x}n\right)\hat{x} + \left(k_{y0} + \frac{2\pi}{d_y}m\right)\hat{y}.\end{aligned} \tag{14}$$

The FW-current coefficients $I_{nm,x}$, $I_{nm,y}$ are proportional to the electric field $\mathbf{E}_{inc}$ of the incident plane wave and, therefore, can be rewritten as $\mathbf{I}_{nm} = (I_{nm,x}\hat{x} + I_{nm,y}\hat{y}) = \underline{\underline{\mathbf{Y}}}_{mn} \cdot \mathbf{E}_{inc}$.

1) Far-Field: Following the procedure in [38] and [39], one can find a form of the far-field pattern in the direction $\hat{\mathbf{r}} = u\hat{x} + v\hat{y}$ that eventually only depends on the position of the vertexes. To this end, let us assume that the ith vertex of the polygonal RIS is in position $\mathbf{r}_v^{(i)}$ at the confluence of two edges aligned along $\mathbf{e}^{(i-1)}, \mathbf{e}^{(i)}$, respectively, both of them with amplitude equal to the side of the polygon (see Fig. 7). The index $i = 1, \ldots, N$ denotes both edges and vertexes, with $\mathbf{r}_v^{(i)} = \mathbf{e}^{(i+1)} - \mathbf{e}^{(i)}$ and $\mathbf{e}^{(N+1)} = \mathbf{e}^{(1)}$ by

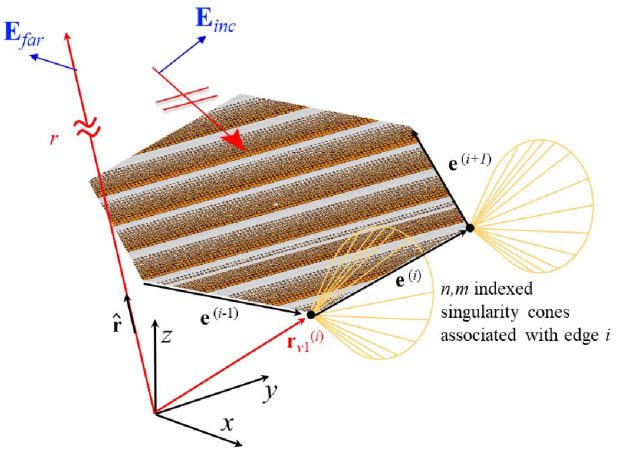

Fig. 7. *Geometry of the polygonal contoured RIS and cone of singularities in the far-field associated with the mn-indexed FW estimated by the infinite canonical problem.*

definition. The field $\mathbf{E}_{far}$ at a distance $r > 2D^2/\lambda$, where D is the maximum dimension of the RIS and λ is the free space wavelength, is given by

$$\mathbf{E}_{far} = \frac{e^{-jkr}}{r}\sum_{i=1}^{N} e^{j\mathbf{K}_{nm}\cdot\mathbf{r}_v^{(i)}}\left(\sum_{n,m}\underline{\underline{\mathbf{D}}}_{v,nm}^{(i)}\right)\cdot\mathbf{E}_{inc} \tag{15}$$

$$\underline{\underline{\mathbf{D}}}_{v,nm}^{(i)} = -\underline{\underline{\mathbf{G}}}_{E,J}(\mathbf{k}_{nm})\cdot\underline{\underline{\mathbf{Y}}}_{nm}\frac{\left(\mathbf{e}^{(i)}\times\mathbf{e}^{(i-1)}\right)\cdot\hat{\mathbf{n}}}{\mathbf{K}_{nm}\cdot\mathbf{e}^{(i)}\mathbf{K}_{nm}\cdot\mathbf{e}^{(i-1)}} \tag{16}$$

where $\hat{\mathbf{n}}$ is the normal to the RIS surface,

$$\mathbf{K}_{nm} = (\mathbf{k}_{nm} - k\hat{\mathbf{r}}) \tag{17}$$

and $\underline{\underline{\mathbf{G}}}_{E,J}(\mathbf{k})$ is the pertinent spectral dyadic Green's function.

Equation (15) represents the summation of field contributions radiated by the FW-induced current sheets associated with the canonical infinite problem, windowed on the RIS aperture. It is represented by diffraction contributions from the vertexes of the polygonal rim. Each vertex diffraction coefficient is a summation of contributions $\underline{\underline{\mathbf{D}}}_{nm}^{(i)}$ associated with the *nm*-indexed FW-induced current. These coefficients exhibit singularities in direction $\hat{\mathbf{r}}$ located on the surface of cones with axes on the two edges confluent to the corners and semiaperture equal to the angles between the two edges and the vectors $\mathbf{K}_{nm} = (\mathbf{k}_{nm} - k\hat{\mathbf{r}})$. We observe that the singularities do not exist for all the indexes *nm*, but only for those *nm*-indexed FWs whose phase velocity along the edge is faster than the speed of light (normally only few of them). The singularities of the vertex diffraction coefficients of each couple of contiguous vertexes compensate for each other, thus giving a well-behaved field everywhere. The numerical impairment

associated with the cancellation of singularities can be overcome by an *a priori* summation of contributions in the critical directions. For instance, the *nm*-indexed diffraction coefficient at edge i can be combined with the one at edge $i+1$ giving a well-behaved field everywhere in space [38], [39]. For rectangular RISs, the combination of the infinities recovers the expression given in [38].

2) Ray Description in the Fresnel Region: For observations in the Fresnel region ($r < 2D^2/\lambda$), and far from the reactive region, the field is obtained by summation of contributions of the direct "visible" FWs (namely, those whose wavenumbers are in the visible spectral region) plus FW-induced edge and vertex diffracted ray contributions from the contour, i.e.,

$$\begin{aligned}\mathbf{E}(\mathbf{r}) &\sim \sum_{i=1}^{N} \frac{e^{-jk|\mathbf{r}-\mathbf{r}_v^{(i)}|}}{k|\mathbf{r}-\mathbf{r}_v^{(i)}|} \sum_{n,m} \underline{\underline{\mathbf{D}}}_{v,nm}^{(i)} T_{v,nm}^{(i)} \cdot \mathbf{E}_{inc} \\ &+ \sum_{i=1}^{N} \left[\sum_{n,m} \frac{e^{-jk|\mathbf{r}-\mathbf{r}_{e,nm}^{(i)}|}}{\sqrt{k|\mathbf{r}-\mathbf{r}_{e,nm}^{(i)}|}} F_{e,nm}^{(i)} \underline{\underline{\mathbf{D}}}_{e,nm}^{(i)} U_{e,nm}^{(i)} \right] \cdot \mathbf{E}_{inc} \\ &+ \left[\sum_{n,m} \underline{\underline{\mathbf{G}}}_{E,J}(\mathbf{k}_{nm}) \cdot \underline{\underline{\mathbf{Y}}}_{nm} U_{nm} e^{-jk|\mathbf{r}-\mathbf{r}_{nm}^{(i)}|} \right] \cdot \mathbf{E}_{inc} \end{aligned} \tag{18}$$

where $\underline{\underline{\mathbf{D}}}_{v.nm}^{(i)}$ and $\underline{\underline{\mathbf{D}}}_{e,nm}^{(i)}$ are vertex and edge diffraction coefficients, respectively, associated with each FW, and $F_{v,nm}^{(i)}$ and $T_{v,nm}^{(i)}$ are transition functions based on Fresnel functions [41], [42] and generalized Fresnel functions [44]–[49]. Equation (18) casts the scattering from the RIS in a ray-type format, which is well suited to be introduced in a conventional ray-tracer for the network planning of a smart environment. We note that, although the summation in (18) can be extended to all the FW associated with the infinite problem, only the ones in the visible region can be included in the approximation since the others are attenuated exponentially in the direction normal to the surface and also produce negligible diffraction effect at the edges.

The last term in (18) represents the direct FW ray fields emanating from the "nonspecular" reflection points $\mathbf{r}_{nm}$ inside the surface. In a "perfect" design of the RIS, only the FW associated with the anomalous reflection has to be considered since all the $\mathbf{I}_{nm}$ coefficients are zero except the one associated with the nonspecular desired direction.

This contribution exists only when the observation point is inside a certain region of space delimited by the existence function U_{nm}, which is the projection of the RIS polygon in the direction of propagation of the *nm*th FW. The FW-induced edge diffracted rays emanate from edge diffraction points $\mathbf{r}_{e,nm}^{(i)}$ whose position can be found through the generalized Fermat principle. Their existence field is regulated by the unit-step function $U_{e,nm}^{(i)}$ that intervenes forcing to zero the diffracted ray when the edge

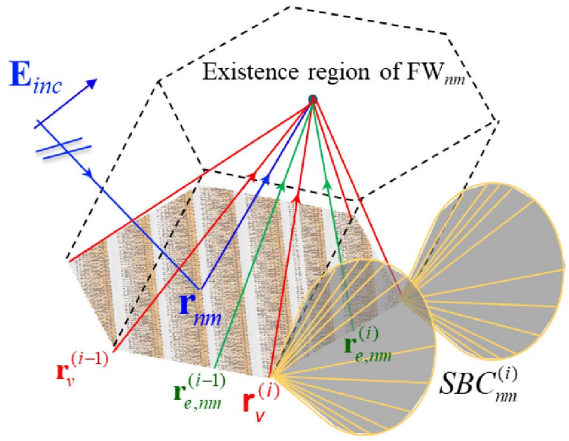

Fig. 8. *Ray contributions for the scattering by a nonspecular reflective RIS in the Fresnel region. The existence region of FW contribution and the shadow boundary cones of edge i are also indicated.*

diffraction point $\mathbf{r}_{e,nm}^{(i)}$ slides out from the edge at the vertexes i or $i+1$, namely, when the observation point crosses the shadow-boundary cones (SBCs) depicted in Fig. 8. The transition functions $F_{v,nm}^{(i)}$ and $T_{v,nm}^{(i)}$ compensate for the discontinuities of the FW and FW-induced edge diffracted field contributions, respectively, appropriately changing their spreading factor and leading to a uniform field everywhere in space.

B. Analysis of SW-Based MTS Sensors and Antennas

In the case of SW-based MTS antennas and sensors, the equivalent impedance is generally modulated along the radial direction. It is convenient to vary the modulation parameters across the aperture to improve the performance. This implies that the overall structure is not rigorously periodic but only "locally periodic" [see Fig. 5(a)]. Accordingly, the analysis of these structures can be performed by using an adiabatic extension of the rigorous FW expansion introduced in Section III-B, which is referred to the 1-D problem which locally matches the 2-D structure. This approach, named the flat optics (FO) method, is described in [51], where its accuracy in the representation of the local currents flowing in the MTS is demonstrated.

We assume that there are no losses in the grounded dielectric characterized by constant relative permittivity ε_r and thickness h, the elements are also lossless, and the available circular aperture has radius a. The MTS top film constituted by the subwavelength metallic elements is modeled as a penetrable BC in the transverse transmission line model [see Fig. 4(b)] and is represented by a modulated equivalent capacitive reactance that is locally periodic, as shown in Fig. 5(b).

It is convenient to adopt a cylindrical coordinate reference system (ρ, ϕ) with unit vectors $(\hat{\boldsymbol{\rho}}, \hat{\boldsymbol{\varphi}})$ [see Fig. 5(b)], whose origin is centered at the feeder position, usually in the geometrical center of the aperture. The metallic

film top covering the MTS imposes the BC in (2) with a homogenized impedance tensor $\underline{\underline{\mathbf{Z}}}_s = j\underline{\underline{\mathbf{X}}}$; the currents flowing into it are denoted by **J**. The tensor $\underline{\underline{\mathbf{X}}}$ is expressed as

$$\underline{\underline{\mathbf{X}}} = \hat{\boldsymbol{\rho}}\hat{\boldsymbol{\rho}} X_{\rho\rho} + (\hat{\boldsymbol{\rho}}\hat{\boldsymbol{\varphi}} + \hat{\boldsymbol{\varphi}}\hat{\boldsymbol{\rho}})\, X_{\rho\varphi} + \hat{\boldsymbol{\varphi}}\hat{\boldsymbol{\varphi}} X_{\varphi\varphi} \tag{19}$$

$$X_{\rho\rho} = \bar{X}_\rho \left[1 + m_\rho(\boldsymbol{\rho}) \cos\left(Ks(\boldsymbol{\rho}) + \Phi_\rho(\boldsymbol{\rho})\right)\right] \tag{20}$$

$$X_{\rho\varphi} = \bar{X}_\rho m_\varphi(\boldsymbol{\rho}) \cos\left(Ks(\boldsymbol{\rho}) + \Phi_\varphi(\boldsymbol{\rho})\right) \tag{21}$$

$$X_{\varphi\varphi} = \bar{X}_\varphi \left[1 - m_\rho(\boldsymbol{\rho}) \cos\left(Ks(\boldsymbol{\rho}) + \Phi_\rho(\boldsymbol{\rho})\right)\right] \tag{22}$$

where the components of $\underline{\underline{\mathbf{X}}}$ feature a constant average value on the aperture. The average reactance in front of the square parentheses is capacitive and homogeneous on the aperture, and K is a large constant that implies the condition on the transverse gradients $K|\nabla_t s| \gg |\nabla_t \Phi_{\rho,\varphi}|$. Note that the function s is slowly variant w.r.t. the wavelength. The different modulation parameters in (19)–(22) are employed and tailored to control the SW interaction with the surface; in particular, it can be noticed that the factor $K_S(\boldsymbol{\rho})$ represents a quickly varying phase contribution that determines the phase of the -1 indexed FW, whereas the term $\Phi_{\rho,\varphi}(\boldsymbol{\rho})$ has much slower variation and controls the aperture field polarization; finally, the modulation index $m_{\varphi,\rho}$ determines the leakage rate of the radiating mode and has a major impact on the aperture illumination and efficiency. It is important to note that all these parameters enable an independent control on the desired aperture field.

The reactance modulation functions that we are dealing with are characterized by a *constant average* value $\hat{X}_\rho$; this ensures that the average current flowing in the coating can be treated as a perturbation of the SW current that would be excited by the source in a nonmodulated surface characterized by its average. It is, thus, introduced a proper modification of the SW current to represent the zeroth indexed term of the adiabatic Floquet modal expansion. On an inductive nonmodulated "opaque" surface, the SW current can be expressed as

$$\mathbf{J}_0 = J_0 H_1^{(2)}(\beta_{\text{sw}}\rho)\, \hat{\boldsymbol{\rho}} \tag{23}$$

where $H_1^{(2)}$ is the Hankel function of second kind and first order. In (23), β_{sw} is the wavenumber of the characteristic mode determined by solving a dispersion equation relevant to the isotropic constant penetrable coating having an impedance equal to $\bar{X}_\rho$; this can be expressed as $\beta_{\text{sw}} = k(1 + \bar{X}_{\text{op}}^2/\zeta^2)^{1/2}$, where $\bar{X}_{\text{op}}$ is the opaque reactance at the resonance, namely, the ratio between total magnetic and electric fields seen at the top interface, and k and ζ are the free space wavenumber and impedance, respectively. A closed-form approximation of the resonant reactance is available in [50]. When a reactance is added to the average reactance, the dominant zeroth Floquet mode is derived from the vectoral form of (12) by a *local* transformation of the unperturbed β_{sw} into a complex wavenumber accounting for the LW propagation and its radial power leakage, which reads $k^{(0)} = \beta_{\text{sw}} + \beta_\Delta - j\alpha$. The wave attenuation parameter $\alpha = \alpha(\boldsymbol{\rho})$ accounts for the SW-to-LW power transfer due to progressive radiation, while the field travels toward the structure edge, $\beta_\Delta = \beta_\Delta(\boldsymbol{\rho})$, accounts for a small deviation in the dominant mode wavenumber due to the local reactance. Notice that both these two terms directly depend on the *local* modulation tensor $\underline{\underline{\mathbf{X}}}$. It is also important to notice that $k^{(0)}$ is a spatially variable complex wavenumber, and the *global* phase of the dominant mode can then be retrieved by integrating $k^{(0)}$. The adiabatic Floquet modes (AFMs) for the currents flowing into the coating can, thus, be obtained using local modes

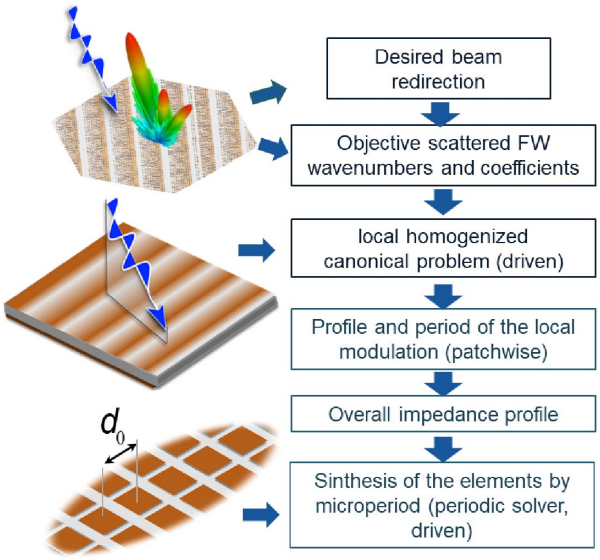

Fig. 9. *Flowchart of the synthesis procedure for reflective MTSs.*

$$\mathbf{J}^{(n)} = \left(J_\rho^{(n)}\hat{\boldsymbol{\rho}} + J_\varphi^{(n)}\hat{\boldsymbol{\phi}}\right) e^{-jnKs(\boldsymbol{\rho})} H_1^{(2)}\left(\int_0^\rho k^{(0)} d\rho'\right). \tag{24}$$

By considering the asymptotic form of the Hankel function, it is clear that any nth mode in (24) is characterized by a curvilinear wavefront that propagates with the *local* n-indexed Floquet mode wavevector

$$\begin{aligned}\boldsymbol{\beta}^{(n)} &= \text{Re}\nabla_t \left[\int_0^\rho k^{(0)} d\boldsymbol{\rho}' + nKs\right] \\ &= (\boldsymbol{\beta}_{\text{sw}} + \boldsymbol{\beta}_\Delta)\, \hat{\boldsymbol{\rho}} + nK\nabla_t s.\end{aligned} \tag{25}$$

This leaks energy at the rate dictated by $\alpha(\boldsymbol{\rho})$.

V. MTS SYNTHESIS

A. Synthesis of Nonspecular Reflectors

The synthesis procedure for nonspecular reflectors is shown in Fig. 9. It starts from the coverage requirements, which dictate the modulation direction and period, and the desired scattered beam amplitudes. The approach

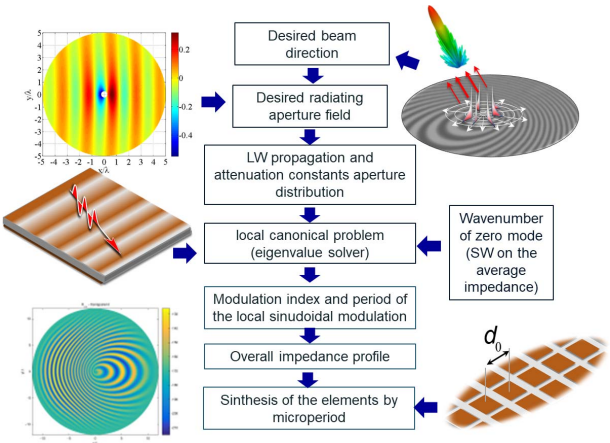

Fig. 10. *Flowchart of the synthesis procedure for SW-based MTS antennas and sensors.*

presented in Section IV-A represents an efficient tool for the accurate evaluation of the scattered field for a generic piecewise polygonal periodic surface and an arbitrary observation domain (either in the Fresnel or far-field zone), and therefore, it can be effectively embedded in a synthesis procedure for the determination of the required FW coefficients for each polygonal patch.

Once the desired FW coefficients are known, one can proceed to the design of the impedance profile using an iterative procedure based on the model proposed in Section III-B. This step must be done having in mind the structure for the MTS practical implementation. In fact, depending on the available status for the single MTS elements, this profile will be continuous or step-like. Typically, continuous profiles can be used for static MTSs or MTSs with continuously tunable elements (e.g., varactors), while step-like profiles are the only option for reconfigurable elements based on switches (e.g., diodes). Finally, the resulting impedance profile will be implemented through practical elements, as explained in Section V-C.

B. Synthesis of MTS Antennas and Sensors

The synthesis of MTS antennas and sensors follows the steps described in Fig. 10. For the sake of simplicity, we refer here to the case of a transmitting antenna, implying that the same procedure can be also applied to receiving antennas and sensors.

For a transmitting antenna, the requirements are normally given for the radiation pattern, which is associated with a certain aperture distribution. Several techniques are available in the literature to make this step, and we will not describe them here. The successive step consists of the identification of the radiating field with the -1 indexed term of the generalized FW expansion associated with the periodic modulation of the MTS. Based on this identification, it is possible to translate the aperture field distribution into the corresponding distributions of the LW attenuation constant, propagation constant, and field polarization, as explained in [51]. Starting from these distributions and from the knowledge of the average impedance, it is possible to define at each aperture point the local impedance modulation able to excite the LW with the desired characteristics. Once the impedance profile is known, the last step consists of its practical implementation through microperiod printed elements (see Section V-C).

C. MTS Implementation Through Printed Patches

In patch-based MTSs, modulation is realized by gradually changing the size, shape, or orientation of the patches in adjacent unit cells. A local "micro"periodicity approximation is used for the practical MTS implementation. More specifically, different unit cells are studied in a periodic environment to construct a database relating the equivalent impedance to one or more parameters characterizing the unit cell. For static MTSs, geometrical parameters with a continuous variation can be used. For reconfigurable MTS, a given geometry is normally analyzed for different status of a tunable material or active component(s) embedded in the unit cell. This provides a discrete set of impedance values available for the synthesis of the desired profile. In both cases, the basic tool for the MTS implementation is represented by the (continuous or discrete) maps relating some unit cell parameters to the corresponding impedance values. The desired impedance profile is sampled at the center of the unit cells, and for each unit cell, the element that best fits the desired impedance value is selected. For anisotropic metasurfaces described by a tensor impedance, maps are generated for all the tensor entries, and the synthesis is performed based on a least-squares minimization involving all the entries.

VI. NUMERICAL RESULTS FOR ANOMALOUS REFLECTION

A. Far-Field Example

This section presents some numerical results illustrating the improved accuracy of the analysis approach introduced in Section III with respect to a local model of the MTS. According to the local approach, the impedance profile of an anomalous reflector is designed to provide a reflection phase linearly varying to compensate for the phase mismatch between the incident and reflected waves, assuming that the local reflection coefficient is the same as the corresponding homogeneous MTS. This leads to the following impenetrable impedance expression for incidence in the yz plane:

$$Z(y) = jZ_0 \cot\left[\frac{ky}{2}(\sin\theta_i - \sin\theta_r)\right] \tag{26}$$

where Z_0 is the wave impedance of the impinging wave, while θ_i and θ_r are the incidence and reflection angles, respectively. According to the local description, this impedance profile provides a single beam in the desired

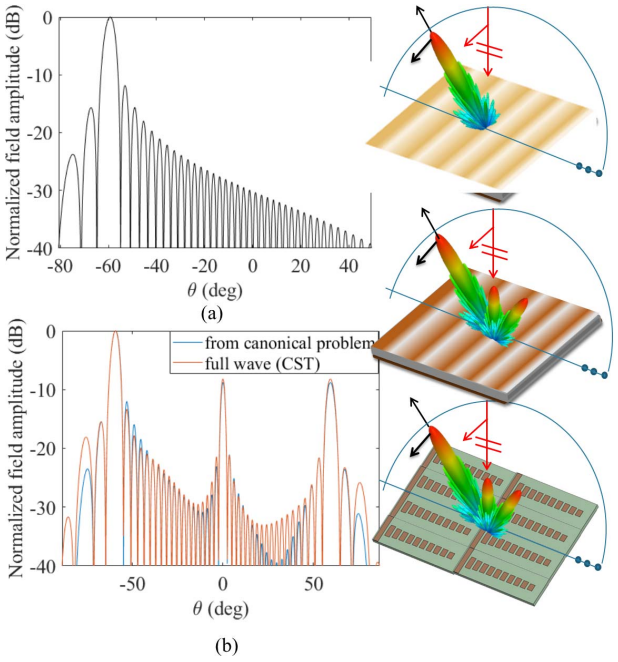

Fig. 11. *Far-field scattered by an MTS characterized by the impedance modulation in (26) implemented through a penetrable impedance on a grounded slab: (a) local approximation and (b) comparison between the model of Section III-B and full-wave simulations associated with the elements in the bottom-right inset.*

direction, corresponding to the -1-indexed FW, as shown in Fig. 11(a), for the case of incidence angle $\theta_i = 0^\circ$ and reflection angle $\theta_r = 60^\circ$.

The results are relevant to the far-field scattered in the incidence plane for a TE-polarized wave impinging on a 20-period-long MTS, assuming a windowing of the currents over a rectangular area. We have then analyzed this scattering problem with the procedure presented in Section III-B. The impedance profile in (26) has been obtained through a modulated penetrable impedance over a grounded dielectric slab of 1.524-mm thickness and a relative permittivity of 9.8 at the operative frequency of 10 GHz. The resulting scattered far-field, as reported in Fig. 11, exhibits two undesired lobes, corresponding to the 0-indexed (specular reflection) and $+1$-indexed FWs, thus revealing the limits of the local design approach.

To verify the accuracy of the analysis in the description of real problems, the penetrable impedance has been synthetized through 12 rectangular metallic patches, as shown in the inset of Fig. 11. The constituent unit cells have the size of 2.9 mm along the periodicity direction and 11.2 mm in the orthogonal direction. The width of all the rectangular patches is equal to 2 mm, while the length is varied to reproduce the desired impedance profile. The resulting structure has been analyzed with the commercial full-wave solver CST. The results are compared in Fig. 11(b). As can be seen, the actual behavior of the structure is well predicted by the proposed model, as opposed to the local description.

As a matter of fact, it has been shown in [53]–[55] that perfect nonspecular reflection (with no other FW modes excited) without cross-polarization can only exist in the case of retroreflection, i.e., wave reflected toward the incidence direction. On the other hand, it is possible to define a continuous tensor impedance profile performing perfect reflection along with polarization conversion for any arbitrary couple of incidence and reflection angles [54], [55]. In particular, Yepes *et al.* [55] provide the expression of the penetrable impedance over a grounded slab exhibiting such behavior, which can be readily implemented through printed elements.

An example corresponding to normal TE-polarized incidence and TM-polarized reflection at -40° is illustrated in Fig. 12. The dielectric slab and the design frequency are the same as in the previous example, and the period is discretized into eight unit cells, each containing a double-anchor-shaped metallic element. As can be seen, the specular reflection ($\theta = 0^\circ$) is very weak. The residual lobe at $+40^\circ$, corresponding to the $+1$ FW, is due to the impedance profile discretization and to some approximations in the reconstruction of the tensor impedance entries profiles.

B. Fresnel Region Ray-Field Example

Representing the ray field in the Fresnel zone is an important issue in smart environment since, not always, the observer is in the far zone of the RIS. In order to show the accuracy of the ray description in the Fresnel region, the formulation in (18) has been applied to a hexagonal array of small dipoles in the free space illuminated by a plane wave. The electric dipoles are oriented along x and have a periodicity of 0.6λ along two axes squinted of 60°. The incident plane wave is coming from the direction $\hat{\mathbf{k}}_{inc} = ((1/2)\hat{y} + \hat{z})(\sqrt{3}/2)$ with an electric field polarized along x. For simplicity, the currents induced on the dipoles

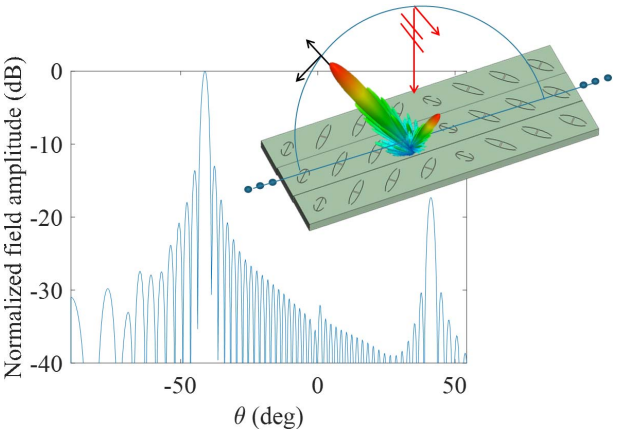

Fig. 12. *Full-wave results for the far-field scattered by an MTS performing anomalous reflection at -40° for normal incidence designed according to the theory presented in [55] and implemented through metallic patches.*

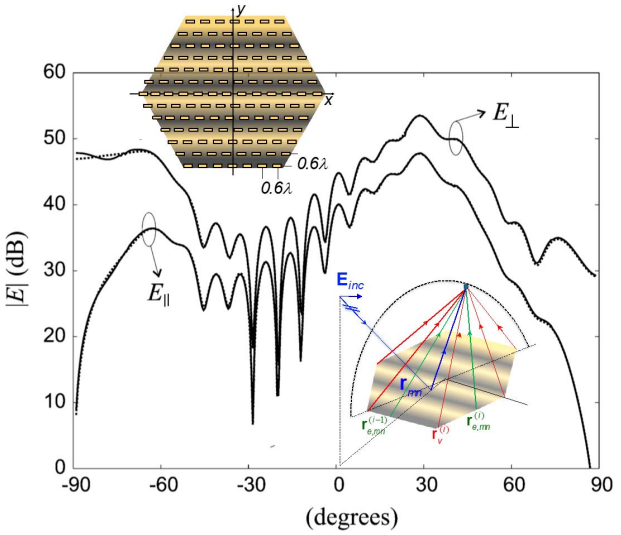

Fig. 13. *Far-field scattered in the Fresnel region by an array of dipoles in the near zone calculated by summation of individual scatterers (dotted line) and by FW and FW-induced diffracted rays (continuous line) with uniform transition functions. The calculations have been performed by A. Cucini (WaveCom).*

are just taken proportional to the incident electric field (no coupling is assumed between the dipoles, namely, the matrix $\mathbf{Y}_{nm}$ in (18) is assumed to be the identity). Fig. 13 compares the results obtained by simply summing the dipole contributions and using a ray-field description, showing excellent accuracy.

VII. PRACTICAL EXAMPLES OF SW-BASED MTS

In this section, we present examples of high-performance MTS antennas that have been designed with the method seen before, realized and measured.

A. High Efficiency

An MTS antenna with maximum aperture efficiency can be designed by implementing the modulation profile introduced in [60]. A Ka-band prototype antenna has been designed and fabricated to verify this approach.

The antenna features a diameter of 27λ at the center frequency of 29.75 GHz. It was designed to radiate a boresight beam with a product between the tapering and spill-over efficiencies of 85%. The prototype was realized by using a Rogers RO3003 laminate characterized by a thickness of 0.762 mm and a relative dielectric constant equal to 3.0 with a loss factor equal to $\tan\delta = 0.001$. The measured peak gain was equal to 37 dBi corresponding to an overall efficiency $\varepsilon_{\text{tot}} \approx 0.70$, including the launching efficiency of SW by the dipole and the losses. This antenna currently constitutes a benchmark in terms of the maximum efficiency attained by MTS apertures. The simulated and measured copolar and cross-polar gain patterns are shown in Fig. 14(a) and (b). The measured patterns are compared with those produced by the analysis based on the AFMs [51], by the Gaussian ring MoM code based on continuous BCs [61], and by a fast multiple method (FMM analysis) [63], which accounts for the actual pixelated layout. Fig. 14(a) and (b) also shows excellent agreement of the measured and simulated results predicted by the mentioned analysis methods.

B. Tilted Beam

Fig. 15 presents a comparison between the simulated and measured gain patterns at 20 GHz of a modulated MTS antenna designed to radiate an RHCP beam that is tilted 30° off from boresight. The antenna has a radius of 10 λ at the working frequency. An excellent agreement between the measured gain patterns and the calculated ones is obtained, corroborating the effectiveness of the design procedure. The achieved peak gain is equal to 33 dBi and corresponds to an aperture efficiency of 0.58. The polarization purity is extremely good. Fig. 15 also shows the overall antenna layout and some details of the feeder, which was composed essentially of a coaxial guide coupled to some patches of annular shape for matching purposes.

C. Very High Gain

An example of a very-high-gain MTS antenna prototype obtained by an appropriate shape of the modulation is

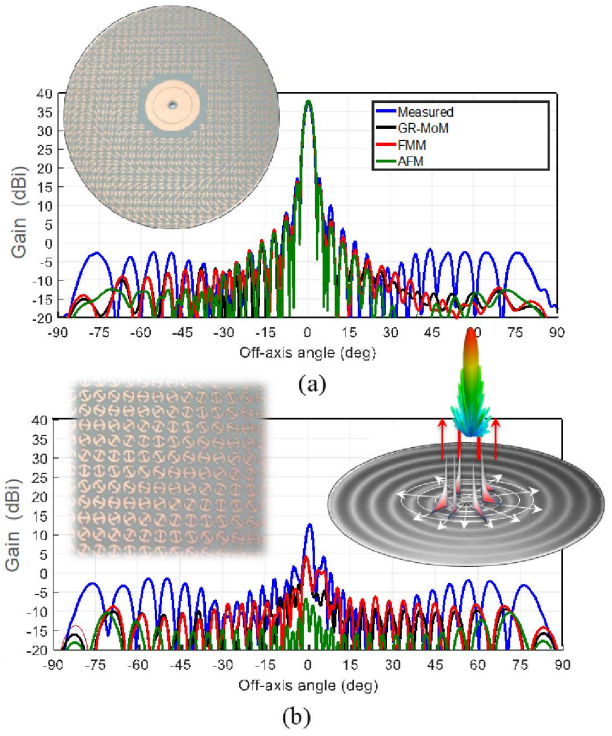

Fig. 14. *Layouts and performance of a highly efficient MTS antenna. (a) Copolar and (b) Cross-polar gain patterns. The curves provide a comparison of the measurements (blue lines) with three different numerical analysis results. Green lines: AFM method. Gray lines: GR-basis function continuous impedance BCs MoM. Red line: full-wave FMM for the textured layout.*

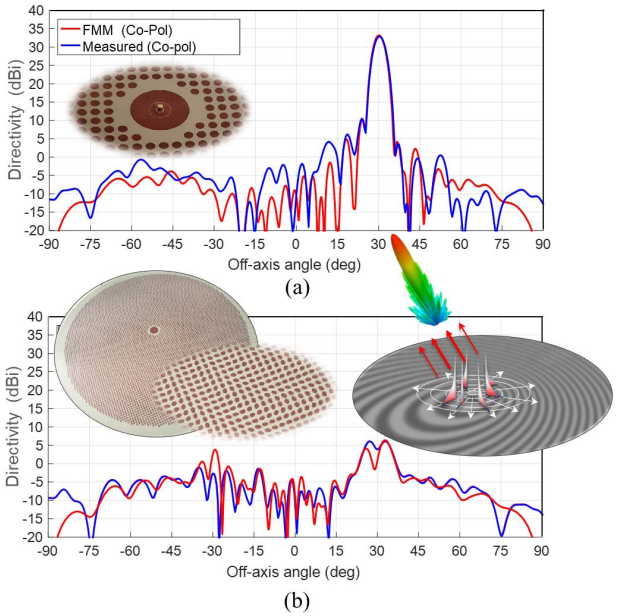

Fig. 15. ***Comparisons between the measured and simulated gain patterns of a tilted beam high-efficiency MTS antenna realized by the "grain of rice" elements. The antenna has been designed to radiate a tilted RHCP beam pointed at 30° at 20 GHz. (a) Copolar component. (b) Cross-polar component. Insets: photographs of the antenna that includes the details of the aperture implementation and the feeder.***

shown in Fig. 16. It attained the largest gain that has been measured until now with this type of antenna. The prototype was designed to operate at 30 GHz and was fabricated using a Rogers RO3003 substrate of 0.762 mm thickness with a 46-cm diameter. The feeder consisted of a coaxial square-flanged connector placed at the center of the antenna that was surrounded by metallic rings on the MTS side. This configuration achieved both a low input reflection coefficient and a high SW launching efficiency.

The measured gain patterns of the antenna are shown in Fig. 16. The peak value reached 39.5 dBi at 30 GHz. The corresponding peak directivity was 41.2 dBi. The losses of this antenna did not exceed 1.7 dB across the operational bandwidth of 500 MHz (5%). It is an unprecedented value for an MTS antenna. This value also includes the losses in the SMA connector. The achievement of this performance is obtained by using the optimal mathematical modulation function presented in [60] as an initial step.

D. Large Bandwidth

A technique to enlarge the operative bandwidth of an MTS antenna consists of radially modifying the modulation periodicity, i.e., the periodicity becomes a function of the radial coordinate. Its values are chosen according to the SW frequency dispersion. The antenna can then be conceived as an active region device where different annular rings are characterized by their own local period and are activated alternately as the frequency is changed to radiate a beam in the desired direction.

Fig. 17 illustrates these mechanisms and the annular active regions of a wideband MTS antenna. The directivity patterns are color-coded to the active regions that produce them. Note that the active region slides inward on the aperture away from its edge as the working frequency increases. This phenomenon is due to a local resonance that couples the SW power with the LW power. Conversely, the aperture area outside of an active region barely interacts with the SW at certain frequencies, and hence, it radiates very weakly at them.

A functional wideband design, for instance, for a broadside radiating aperture is ensured by matching the modulation phase $Ks(\rho)$ in (19)–(22) with the frequency-dependent SW phase through radially shaping the periodicity of the modulation function. Note that the vector position of the modulation phase will be assumed to be independent of the azimuthal angle throughout this section. As the SW wavenumber $\beta_{sw}(\omega, \rho)$ depends dominantly on the "opaque" reactance $\bar{X}_{op}(\omega)$ of the MTS antenna, any wideband design needs to take into consideration both the dispersion of the metallic coating and the contribution from the grounded slab over the design bandwidth. Because the dispersion of the capacitive reactance of the metallic coating is quite weak when compared with the one of the grounded slabs, it can be evaluated at a single frequency (usually the central one). The in-band frequency behavior can then be extrapolated with a linear approximation of the capacitive admittance. When needed, a more refined estimation of the texture reactance can be obtained by using the method illustrated in [50]. We note that β_{sw} depends, in the second order, on the amplitude

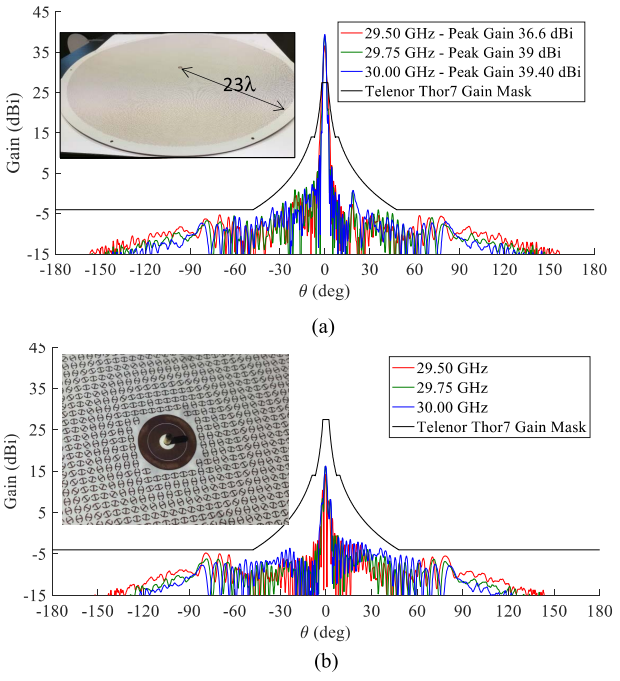

Fig. 16. ***Measured gain pattern of the very-high-gain MTS antenna prototype. (a) Copolar. (b) Cross polar. Inset: details of the feeder (design and measurement done by Wave Up).***

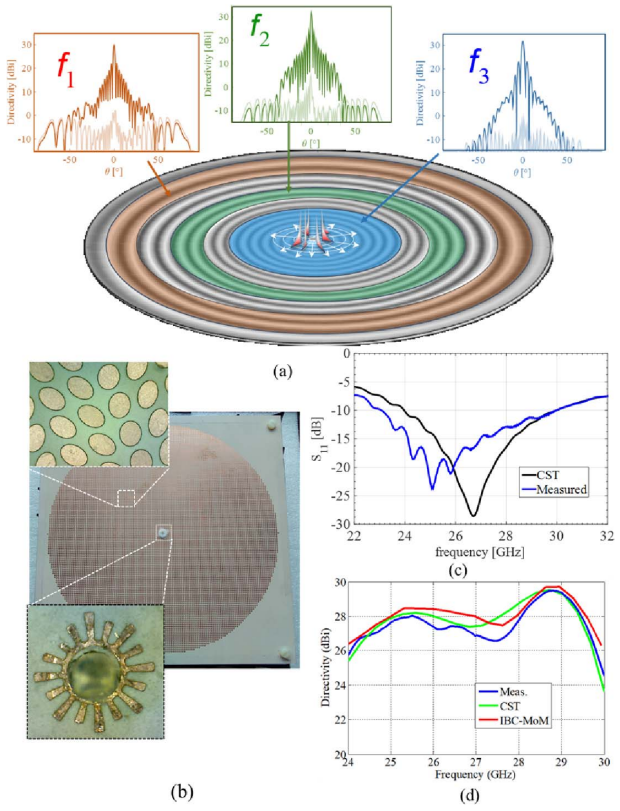

Fig. 17. *Ka-band large bandwidth MTS antenna. (a) Active region principle. (b) Photograph of the fabricated prototype with insets showing the large bandwidth feed and the elliptical patches used to synthesize the impedance tensor. (c) Input impedance. (d) Directivity versus frequency response: measured (blue line) and simulated directivities. The simulated values were computed with the IBC-MoM in [61] (red line) taking into consideration the solution for the ideal homogenized reactance and with the commercial software CST.*

and phase of the impedance modulation, which changes point by point over the surface.

Fig. 17 shows the results for an aperture designed to work at the Ka-band. Its substrate has the thickness $h = 0.635$ mm and the relative permittivity $\varepsilon_r = 6.15$. The modulation is characterized by an exponential profile of the radial periodicity that is bounded at the center and the rim by the values $d_1 = 7.0$ mm and $d_2 = 13.7$ mm, respectively. The antenna has a 3-dB bandwidth ranging from 23.0 to 29.1 GHz and exhibits $\pm$2-dB in-band gain oscillation. Even though the present design is quite effective in extending the operability of MTS antennas in terms of their pattern bandwidths, these gain oscillations with respect to its average are still nonnegligible.

E. Range of Applicability in a Diagram Gain–Bandwidth

The range of operability of MTS antennas in terms of their main performance characteristics is compared with those of other flat microwave antennas in Fig. 18. The diagram represents the obtained gain versus the relative bandwidth. The MTS antennas cover a large region of this diagram. They are able to have not only up to a 40-dB peak gain with few percent bandwidths but also a large bandwidth with medium gain.

F. Aperture Sharing: Multiplexing by Multiport

A major practical goal for the wireless network is to obtain multiple directive beams from a single aperture simultaneously. For SW-based antennas, this aperture sharing concept foresees, in essence, the superposition of two or more modulation functions point by point on the entire aperture. An example of such an MTS antenna was developed in [62] and is illustrated in Fig. 19. In these specific cases, the reactance modulation tensor assumes a more general form of a summation of modulation, which is eventually implemented by printed elements. Assigning one feed point per beam instead of a single, unique feed, allows for multiplexing by a simple switching network. One could consider dividing the aperture in distinct angular sectors, each excited by a different source. This approach requires a feed network scheme in which each source illuminates only its corresponding sector. Consequently, the overall system is more complex in comparison to the single feed version. Nevertheless, one can still apply the superposition of the modulation patterns to obtain one independent beam per source. The main difference is that each modulation will have to be referenced to a local coordinate system whose origin is located at the corresponding feed point location. A practical example with three ports is shown in Fig. 20 where the results of three partially overlapped aperture modulations are realized by printed elliptical subwavelength patches at 4.5 GHz.

A further example of the multibeam antenna at 4GHz is shown in Fig. 21; it consists of a 19-port antenna printed on the same substrate and realized by individual MTS tensors with moderately overlapped impedance modulation. The apertures are circular and about 3.5 wavelength diameter each; they are distributed with centers over a hexagonal lattice. Each aperture has a different layout in such a way to have beams that overlap in the far zone at about

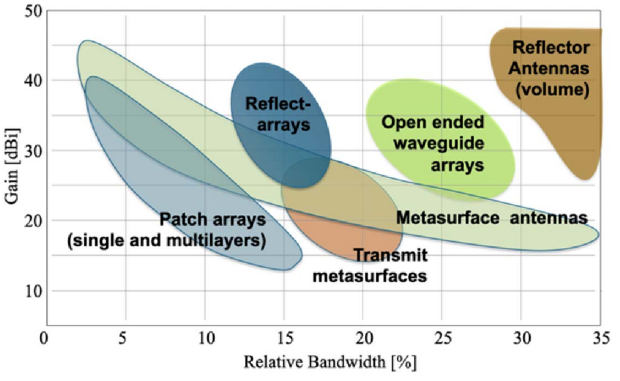

Fig. 18. *Gain versus relative bandwidth diagram for several flat antenna typologies.*

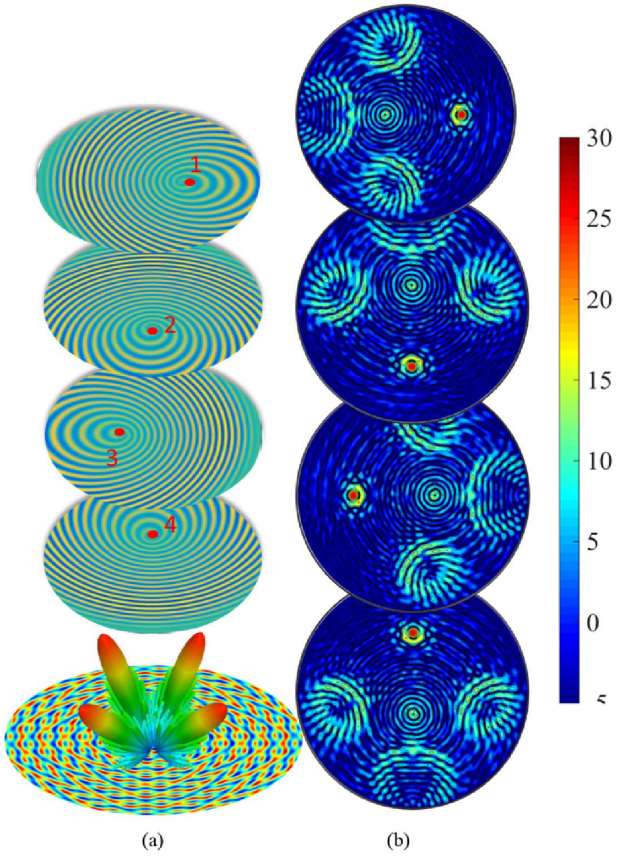

Fig. 19. *Four-beam MTS antenna realized by superimposing the modulation functions. (a) Aperture sharing to generate the four beams using four monopoles and (top left) the superposition of their modulated impedance patterns. The colors on the aperture represent the amplitude of the impedance modulation. (b) Far-field directivity patterns in the uv plane that was obtained with the homogenized-impedance MoM simulations in [61].*

−3 dB. The beams realized by each port are reported in the *uv* plane in the bottom part of Fig. 21. Each beam exhibits a directivity of about 15-dB spanning with −3 dB over a conical angle of ±45° angle. The described structure allows for implementing a very simple MIMO for sensing the environment with extremely low cost. We stress that everything can be obtained by printing all the MTS on the same substrate and connectorizing the back of the substrate.

VIII. CHALLENGES FOR SMART RADIO ENVIRONMENT

Fast reconfigurability of the beam and beam scanning based on dynamic, electronically reconfigurable MTSs are the most impactful challenges for rendering RIS an enabling technology for SRE scenarios. This can be achieved through the inclusion in the MTS of active devices or tunable materials; this way, the electric features of the inclusions become voltage controlled, and hence, the BCs offered by the MTS can be properly adjusted by an external control.

Although this concept has been already demonstrated (see [57], [64], and [69]), existing solutions still need to be improved in terms of efficiency. In fact, active

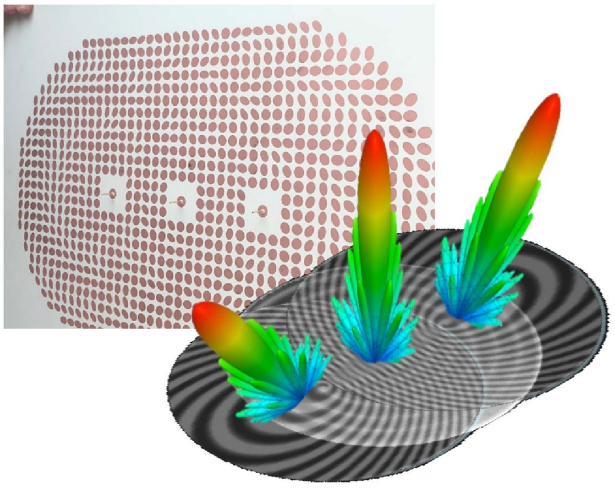

Fig. 20. *Subwavelength elliptical patch implementation of three-beam/three-port MTS antenna at 4 GHz realized by a partial overlap of the modulation functions (designed by Wave-Up and realized by Ultimetas).*

devices and tunable materials yield an increase in the antenna losses with a consequent reduction of gain and increase in power demand; losses become more important when working at higher frequencies (e.g., the Ka-band): frequency scalability is indeed another challenge. Losses become less critical when dealing with mechanical recon-

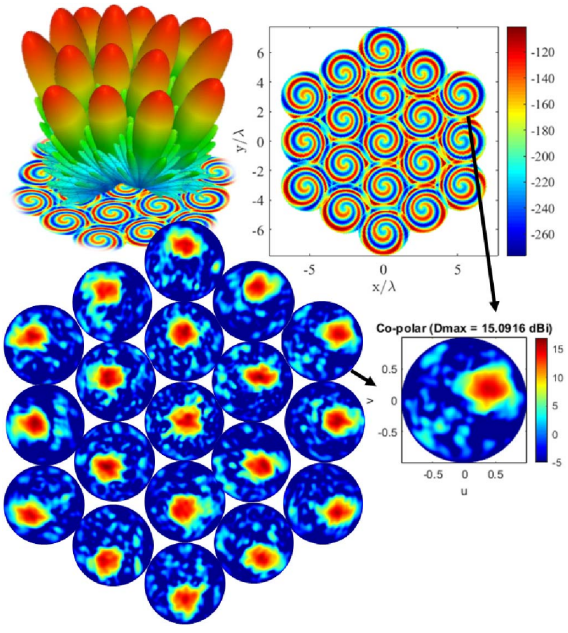

Fig. 21. *Example of multiport/multibeam antenna with MTS printed over a unique substrate. The antenna can realize 19 beams of about 15-dB directivity each. Right corner: layout of one of the entries of the impedance tensor. Bottom: radiated beams directivity maps in the uv plane for each excited port, obtained by a homogenized-impedance full-wave analysis over the entire 19-aperture structure. (Zoomed-in view of one u-v map with the scale is reported on the right.) The position of each u-v contour map is associated with the analogous position of the space aperture layout (see the arrows.)*

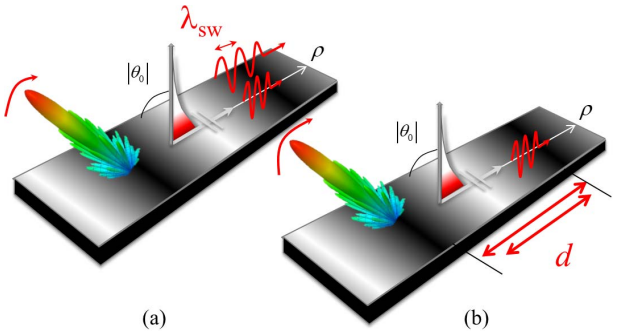

Fig. 22. *Pictorial representation of the possible beam scanning approaches for SW-based antennas. (a) Change of SW wavelength for a fixed period. (b) Change of period for a fixed surface-wave wavelength.*

figuration. The use of micromechanical systems or piezoelectric devices has been proposed, but they may suffer from low reliability, and an MTS antenna based on such devices may be too sensitive to the external vibrations if installed on moving vehicles.

Beam scanning in SW-based reconfigurable MTS antennas can be obtained through two different approaches, illustrated in Fig. 22: the first one is based on the control of the SW wavenumber and the second one on the control of the periodicity. Both allow for a 1-D scanning of the radiated beam. In particular, the first approach allows beam scanning at a fixed frequency with a single voltage control. This approach has been exploited in [70] using liquid crystals as tunable substrates, making use of the formulation presented in [71]. The radiating part is constituted by a parallel plate waveguide partially filled by liquid crystals with gradually modulated, electrically small slots etched on the upper wall, while the feeding network is realized through a pillbox network (see the inset in Fig. 23). The concept was validated through the realization and experimental characterization of an antenna prototype in the Ka-band although only a limited scan range (around 10°) was measured due to an imperfect alignment of the *LC* layer.

Special liquid crystals for microwaves could be extremely beneficial, and some companies are investing in this direction although they are limited in terms of reconfiguration speed. Alternative tunable materials are ferroelectric or phase-changing materials, such as vanadium dioxide. However, phase-changing materials suffer from temperature instability. Advances in phase-changing materials would bring a significant benefit to reconfigurable MTSs, in terms of losses and switching time reduction, as well as an increase in temperature stability.

The second approach [see Fig. 22(b)] is based on the tuning of the modulation period, and therefore, it requires multiple control signals across the MTS. As a difference from the previous approach, these controls can also be binary. If all the MTS unit cells are individually piloted, 2-D scanning can be also achieved through the pointwise control of the MTS modulation. This strategy was applied and experimentally validated in [72] to implement elevation scanning in an array of modulated MTS channels

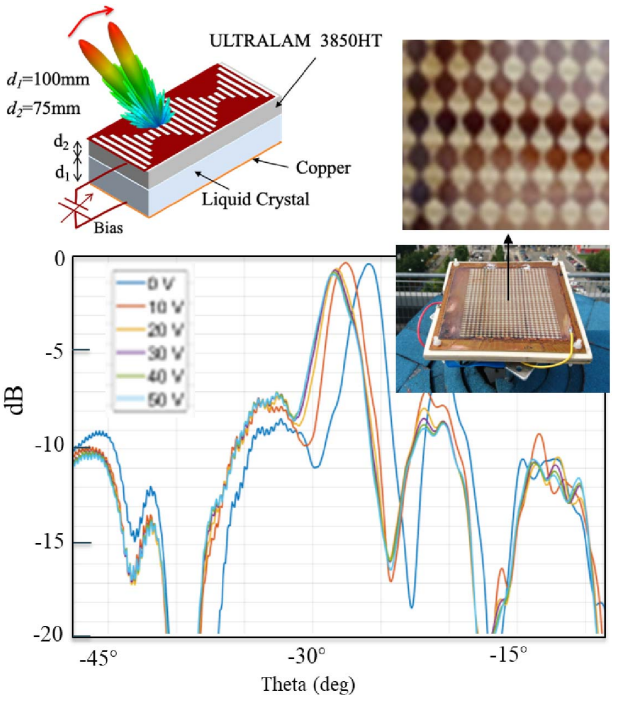

Fig. 23. *Implementation of the approach in Fig. 22(a). Measured radiation pattern from a liquid crystal-based reconfigurable MTS antenna under different bias conditions. The inset shows a picture of the prototype and the geometry.*

for RIS in 5G scenarios. In that case, the pointing angle was precisely controlled by piloting a network of p-i-n diodes connected to metallic dipoles printed on top of a PCB. The basic idea is presented in Fig. 24. MTS with integrated active devices, instead of discrete ones, would bring advantages in terms of reliability, losses, and performance. In this framework, the power consumption for the control network can be decreased by using field-effect transistors instead of p-i-n diodes as switches. However, realizing integrated devices in a wide area will require significant improvement in the accuracy and repeatability of the fabrication processes.

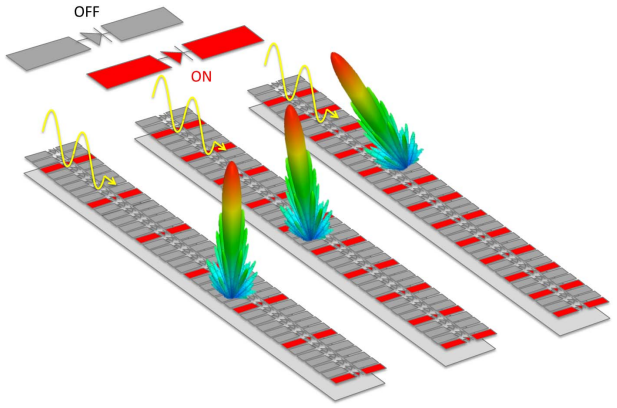

Fig. 24. *Implementation of the approach in Fig. 22(b). Dipole type MTS constituted by printed dipoles with p-i-n diodes in* on *(red dipoles) and* off *(gray dipoles) configurations. Different periods give different radiated beams.*

Alternative strategies for reconfigurability of the RIS consist of optical pumping photosensitive substrate with MTSs printed on top. Silicon or gallium arsenide substrates can be used, together with checkerboard-type self-complementary MTSs' CB-MTS. The vertexes of CB-MTS are disconnected by a small gap in off-conditions, and they are virtually connected by the incident optical power density [73]. Since the gaps are very small (for instance at the level of few optical wavelengths), this allows to modify the MTS configuration with an extremely small power [74].

3-D printing processes are also extremely appealing for MTS antennas, creating the possibility to move beyond the classic PCB processes, offering chances to build up the MTS by adding specific features to the inclusions, and, hence, improving performance at low cost.

Other challenges arise from the complexity and large size of the MTSs required for SREs. Indeed, despite the significant advances done in the development of the design procedures described here, MTS optimization is still a future challenge topic. Whenever strong requirements on performance are demanded, it is necessary to optimize the final MTS layout, which may be composed of up to 100 000 elements. Managing the high number of inclusions with numerical methods, including electronic devices and losses, requires smart strategies, which make combined use of homogenized BCs and fast integral-equation solvers, embedding an accurate model of the tunable elements.

IX. CONCLUSION

This article has reviewed modeling, design, and simulation strategies for MTS-based reflecting surfaces and antennas/sensors, which represents the key enablers for future SREs. Several practical realizations have been shown to illustrate the promising potential of this technology, including overlapping apertures for multibeaming. Fast beam hopping and multibeam operations with low power consumption and low cost are interesting features for SRE. Furthermore, the operation principle of MTS antennas allows for tailoring, in real time, the MTS with active devices or tunable materials. While the initial concern of sometimes ago about bandwidth is a challenge in fast progress, losses, agility, and dynamic speed are still open issues for both design and fabrication technology aspects. Finally, the possibility to easily customize RIS features in the Fresnel zone and describe it in terms of rays opens the possibility of a fast deterministic analysis of the SRE. ■

Acknowledgment

The authors wish to acknowledge the contribution of several people to the results shown in this article: Francesco Caminita (Wave Up Srl, Siena, Italy) for the design of the high efficiency antenna in Fig. 15 and the FMM results, Gabriele Minatti (Wave Up Srl) for the design of the very high-gain antenna in Fig. 16 and the multibeam antenna in Fig. 21, Cristian Della Giovampaola (Wave Up Srl) for the design of the multibeam antennas in Fig. 20 and the measurements in Fig. 16, David Gonzalez-Ovejero (Centre National de la Recherche Scientifique-Institut d'Electronique et des Technologies du numéRique (CNRS-IETR), Rennes, France) for the realization and measurements of the broadband antenna in Fig. 17, the multibeam antenna in Fig. 19, and the continuous impedance boundary condition method of moments (IBC-MoM) results, Marco Faenzi (University of Siena) for the design of the broadband antenna in Fig. 17, Prof. Charlotte Tripon Canseliet (Ultimetas, Paris, France) for the realization of the multibeam antenna in Fig. 20, Alessio Cucini (WaveComm Srl, Siena) for the results in Fig. 13, Cristina Yepes (University of Siena, Siena) for the implementation of the anomalous reflector in Fig. 12, Romeo Beccherelli [Istituto per la Microelettronica e Microsistemi (IMM), Consiglio Nazionale delle Ricerche (CNR)] and Valerio Martorelli (Ingegneria Dei Sistemi) for the realization of the antenna in Fig. 23, and Giorgio Giordanengo (Links) for the measurements of the antenna in Fig. 23.

REFERENCES

[1] C. Liaskos, S. Nie, A. Tsioliaridou, A. Pitsillides, S. Ioannidis, and I. Akyildiz, "A new wireless communication paradigm through software-controlled metasurfaces," *IEEE Commun. Mag.*, vol. 56, no. 9, pp. 162–169, Sep. 2018.

[2] M. D. Renzo *et al.*, "Smart radio environments empowered by reconfigurable AI meta-surfaces: An idea whose time has come," *EURASIP J. Wireless Commun. Netw.*, vol. 2019, no. 1, pp. 1–20, Dec. 2019.

[3] M. Di Renzo *et al.*, "Smart radio environments empowered by reconfigurable intelligent surfaces: How it works, state of research, and the road ahead," *IEEE J. Sel. Areas Commun.*, vol. 38, no. 11, pp. 2450–2525, Nov. 2020.

[4] E. Basar, M. D. Renzo, J. De Rosny, M. Debbah, M. Alouini, and R. Zhang, "Wireless communications through reconfigurable intelligent surfaces," *IEEE Access*, vol. 7, pp. 116753–116773, 2019.

[5] F. Tariq *et al.*, "A speculative study on 6G," *IEEE Wireless Commun.*, vol. 27, no. 4, pp. 118–125, Aug. 2020.

[6] S. B. Glybovski, S. A. Tretyakov, P. A. Belov, Y. S. Kivshar, and C. R. Simovski, "Metasurfaces: From microwaves to visible," *Phys. Rep.*, vol. 634, pp. 1–72, May 2016.

[7] K. Achouri, M. A. Salem, and C. Caloz, "General metasurface synthesis based on susceptibility tensors," *IEEE Trans. Antennas Propag.*, vol. 63, no. 7, pp. 2977–2991, Jul. 2015.

[8] F. Yang and Y. Rahmat-Samii, *Surface Electromagnetics, With Applications in Antenna, Microwave, and Optical Engineering*. Cambridge, U.K.: Cambridge Univ. Press, 2019.

[9] A. Li, S. Singh, and D. Sievenpiper, "Metasurfaces and their applications," *Nanophotonics*, vol. 7, no. 6, pp. 989–1011, Mar. 2018.

[10] T. J. Cui, M. Q. Qi, X. Wan, J. Zhao, and Q. Cheng, "Coding metamaterials, digital metamaterials and programmable metamaterials," *Light, Sci. Appl.*, vol. 3, no. 10, p. e218, Oct. 2014.

[11] C. D. Giovampaola and N. Engheta, "Digital metamaterials," *Nature Mater.*, vol. 13, no. 12, pp. 1115–1121, Sep. 2014.

[12] T. J. Cui, M. Q. Qi, X. Wan, J. Zhao, and Q. Cheng, "Coding metamaterials, digital metamaterials and programmable metamaterials," *Light, Sci. Appl.*, vol. 3, no. 10, p. e218, 2014.

[13] L. Li *et al.*, "Electromagnetic reprogrammable coding-metasurface holograms," *Nature Commun.*, vol. 8, no. 1, p. 197, Dec. 2017.

[14] L. Li and T. J. Cui, "Information metamaterials—From effective media to real-time information processing systems," *Nanophotonics*, vol. 8, no. 5, pp. 703–724, Mar. 2019.

[15] Q. Ma, G. D. Bai, H. B. Jing, C. Yang, L. Li, and T. J. Cui, "Smart metasurface with self-adaptively reprogrammable functions," *Light, Sci. Appl.*, vol. 8, no. 1, p. 98, Dec. 2019.

[16] V. S. Asadchy, M. Albooyeh, S. N. Tcvetkova, A. Díaz-Rubio, Y. Ra'di, and S. A. Tretyakov, "Perfect control of reflection and refraction using spatially dispersive metasurfaces," *Phys. Rev. B, Condens. Matter*, vol. 94, no. 7, Aug. 2016, Art. no. 075142.

[17] P. Nayeri, F. Yang, and A. Z. Elsherbeni, *Reflectarray Antennas: Theory, Designs, and Applications*. Hoboken, NJ, USA: Wiley, 2018.

[18] C. Pfeiffer and A. Grbic, "Millimeter-wave transmitarrays for wavefront and polarization control," *IEEE Trans. Microw. Theory Techn.*, vol. 61, no. 12, pp. 4407–4417, Dec. 2013.

[19] N. Yu *et al.*, "Flat optics: Controlling wavefronts with optical antenna metasurfaces," *IEEE J. Sel. Topics Quantum Electron.*, vol. 19, no. 3, p. 4700423, May/Jun. 2013.

[20] A. M. H. Wong and G. V. Eleftheriades, "Perfect

anomalous reflection with a bipartite Huygens' metasurface," *Phys. Rev. X*, vol. 8, no. 1, Feb. 2018, Art. no. 011036.
[21] A. Epstein and G. V. Eleftheriades, "Huygens' metasurfaces via the equivalence principle: Design and applications," *J. Opt. Soc. Amer. B, Opt. Phys.*, vol. 33, no. 2, p. A31, 2016.
[22] V. G. Ataloglou, M. Chen, M. Kim, and G. V. Eleftheriades, "Microwave Huygens' metasurfaces: Fundamentals and applications," *IEEE J. Microw.*, vol. 1, no. 1, pp. 374–388, Jan. 2021.
[23] S. Maci, G. Minatti, M. Casaletti, and M. Bosiljevac, "Metasurfing: Addressing waves on impenetrable metasurfaces," *IEEE Antennas Wireless Propag. Lett.*, vol. 10, pp. 1499–1502, 2011.
[24] R. Quarfoth and D. Sievenpiper, "Artificial tensor impedance surface waveguides," *IEEE Trans. Antennas Propag.*, vol. 61, no. 7, pp. 3597–3606, Jul. 2013.
[25] R. Quarfoth and D. Sievenpiper, "Surface wave scattering reduction using beam shifters," *IEEE Antennas Wireless Propag. Lett.*, vol. 13, pp. 963–966, 2014.
[26] G. Minatti *et al.*, "Modulated metasurface antennas for space: Synthesis, analysis and realizations," *IEEE Trans. Antennas Propag.*, vol. 63, no. 4, pp. 1288–1300, Apr. 2015.
[27] B. H. Fong, J. S. Colburn, J. J. Ottusch, J. L. Visher, and D. F. Sievenpiper, "Scalar and tensor holographic artificial impedance surfaces," *IEEE Trans. Antennas Propag.*, vol. 58, no. 10, pp. 3212–3221, Oct. 2010.
[28] C. Pfeiffer and A. Grbic, "A printed, broadband Luneburg lens antenna," *IEEE Trans. Antennas Propag.*, vol. 58, no. 9, pp. 3055–3059, Sep. 2010.
[29] M. Faenzi *et al.*, "Metasurface antennas: New models, applications and realizations," *Sci. Rep.*, vol. 9, no. 1, pp. 1–14, Jul. 2019.
[30] S. Maci and A. Cucini, "FSS-based EBG surface," in *Electromagnetic Metamaterials: Physics and Engineering Aspects*, N. Engheta and R. Ziolkowski, Eds. Hoboken, NJ, USA: Wiley, 2006.
[31] M. A. Francavilla, E. Martini, S. Maci, and G. Vecchi, "On the numerical simulation of metasurfaces with impedance boundary condition integral equations," *IEEE Trans. Antennas Propag.*, vol. 63, no. 5, pp. 2153–2161, May 2015.
[32] E. Martini, F. Caminita, and S. Maci, "Double-scale homogenized impedance models for periodically modulated metasurfaces," *EPJ Appl. Metamater.*, vol. 7, p. 12, Jan. 2020.
[33] A. A. Oliner and A. Hessel, "Guided waves on sinusoidally-modulated reactance surfaces," *IRE Trans. Antennas Propag.*, vol. 7, no. 5, pp. 201–208, Dec. 1959.
[34] F. Caminita, E. Martini, and S. Maci, "Exact solution for anisotropic, periodically modulated boundary conditions excited by a surface wave," in *Proc. 9th Eur. Conf. Antennas Propag. (EuCAP)*, Jan. 2015.
[35] N. Yu *et al.*, "Light propagation with phase discontinuities: Generalized laws of reflection and refraction," *Science*, vol. 334, no. 6054, pp. 333–337, Oct. 2011.
[36] Q. Wu, S. Zhang, B. Zheng, C. You, and R. Zhang, "Intelligent reflecting surface-aided wireless communications: A tutorial," *IEEE Trans. Commun.*, vol. 69, no. 5, pp. 3313–3351, May 2021.
[37] J. Budhu and A. Grbic, "Perfectly reflecting metasurface reflectarrays: Mutual coupling modeling between unique elements through homogenization," *IEEE Trans. Antennas Propag.*, vol. 69, no. 1, pp. 122–134, Jan. 2021.
[38] A. Cucini and S. Maci, "A compact formula for the array factor of planar phased arrays with polygonal shape and skewed grid," *IEEE Antennas Wireless Propag. Lett.*, vol. 1, pp. 138–141, 2002.
[39] A. Cucini, "High-frequency Green's function for planar periodic phased arrays with skewed grid and polygonal contour," *IEEE Trans. Antennas Propag.*, vol. 54, no. 12, pp. 3659–3668, Dec. 2006.
[40] A. Diaz-Rubio and S. A. Tretyakov, "Macroscopic modeling of anomalously reflecting metasurfaces: Angular response and far-field scattering," *IEEE Trans. Antennas Propag.*, vol. 69, no. 10, pp. 6560–6571, Oct. 2021.
[41] F. Capolino, M. Albani, S. Maci, and L. B. Felsen, "Frequency-domain Green's function for a planar periodic semi-infinite phased array. I. Truncated floquet wave formulation," *IEEE Trans. Antennas Propag.*, vol. 48, no. 1, pp. 67–74, Jan. 2000.
[42] F. Capolino, M. Albani, S. Maci, and L. B. Felsen, "Frequency-domain Green's function for a planar periodic semi-infinite phased array. II. Diffracted wave phenomenology," *IEEE Trans. Antennas Propag.*, vol. 48, no. 1, pp. 75–85, Jan. 2000.
[43] A. Cucini and S. Maci, "Macro-scale basis functions for the method of moment analysis of large periodic microstrip arrays," *Appl. Comput. Electromagn. Soc. J.*, vol. 21, no. 3, pp. 256–266, Nov. 2006.
[44] F. Mariottini, F. Capolino, S. Maci, and L. B. Felsen, "Asymptotic high-frequency Green's function for a large rectangular planar periodic phased array of dipoles with weakly tapered excitation in two dimensions," *IEEE Trans. Antennas Propag.*, vol. 53, no. 2, pp. 608–620, Feb. 2005.
[45] F. Capolino, S. Maci, and L. B. Felsen, "Asymptotic high-frequency Green's function for a planar phased sectoral array of dipoles," *Radio Sci.*, vol. 35, no. 2, pp. 579–593, Mar. 2000.
[46] S. Maci, F. Capolino, and L. B. Felsen, "Three-dimensional Green's function for planar rectangular phased dipole arrays," *Wave Motion*, vol. 34, no. 3, pp. 263–279, Sep. 2001.
[47] F. Capolino and S. Maci, "Uniform high-frequency description of singly, doubly, and vertex diffracted rays for a plane angular sector," *J. Electromagn. Waves Appl.*, vol. 10, no. 9, pp. 1175–1197, Jan. 1996.
[48] F. Capolino and S. Maci, "Simplified closed-form expressions for computing the generalized Fresnel integral and their application to vertex diffraction," *Microw. Opt. Technol. Lett.*, vol. 9, no. 1, pp. 32–37, May 1995.
[49] M. Albani, F. Capolino, G. Carluccio, and S. Maci, "UTD vertex diffraction coefficient for the scattering by perfectly conducting faceted structures," *IEEE Trans. Antennas Propag.*, vol. 57, no. 12, pp. 3911–3925, Dec. 2009.
[50] M. Mencagli, Jr., E. Martini, and S. Maci, "Transition function for closed-form representation of metasurface reactance," *IEEE Trans. Antennas Propag.*, vol. 64, no. 1, pp. 136–145, Jan. 2016.
[51] G. Minatti, F. Caminita, E. Martini, and S. Maci, "Flat optics for leaky-waves on modulated metasurfaces: Adiabatic Floquet-wave analysis," *IEEE Trans. Antennas Propag.*, vol. 64, no. 9, pp. 3896–3906, Sep. 2016.
[52] G. Minatti, F. Caminita, E. Martini, M. Sabbadini, and S. Maci, "Synthesis of modulated-metasurface antennas with amplitude, phase, and polarization control," *IEEE Trans. Antennas Propag.*, vol. 64, no. 9, pp. 3907–3919, Sep. 2016.
[53] N. M. Estakhri and A. Alù, "Wave-front transformation with gradient metasurfaces," *Phys. Rev. X*, vol. 6, no. 4, Oct. 2016, Art. no. 041008.
[54] V. S. Asadchy, M. Albooyeh, S. N. Tcvetkova, A. Díaz-Rubio, Y. Ra'di, and S. A. Tretyakov, "Perfect control of reflection and refraction using spatially dispersive metasurfaces," *Phys. Rev. B, Condens. Matter*, vol. 94, no. 7, Aug. 2016, Art. no. 075142.
[55] C. Yepes, M. Faenzi, S. Maci, and E. Martini, "Perfect non-specular reflection with polarization control by using a locally passive metasurface sheet on a grounded dielectric slab," *Appl. Phys. Lett.*, vol. 118, no. 23, Jun. 2021, Art. no. 231601.
[56] D. R. Smith, O. Yurduseven, L. P. Mancera, P. Bowen, and N. B. Kundtz, "Analysis of a waveguide-fed metasurface antenna," *Phys. Rev. A, Gen. Phys.*, vol. 8, no. 5, Nov. 2017, Art. no. 054048.
[57] D. F. Sievenpiper, "Forward and backward leaky wave radiation with large effective aperture from an electronically tunable textured surface," *IEEE Trans. Antennas Propag.*, vol. 53, no. 1, pp. 236–247, Jan. 2005.
[58] O. Yurduseven, D. L. Marks, T. Fromenteze, and D. R. Smith, "Dynamically reconfigurable holographic metasurface aperture for a mills-cross monochromatic microwave camera," *Opt. Exp.*, vol. 26, no. 5, pp. 5281–5291, 2018.
[59] M. Li, S. Xiao, J. Long, and D. F. Sievenpiper, "Surface waveguides supporting both TM mode and TE mode with the same phase velocity," *IEEE Trans. Antennas Propag.*, vol. 64, no. 9, pp. 3811–3819, Sep. 2016.
[60] G. Minatti, E. Martini, and S. Maci, "Efficiency of metasurface antennas," *IEEE Trans. Antennas Propag.*, vol. 65, no. 4, pp. 1532–1541, Apr. 2017.
[61] D. González-Ovejero and S. Maci, "Gaussian ring basis functions for the analysis of modulated metasurface antennas," *IEEE Trans. Antennas Propag.*, vol. 63, no. 9, pp. 3982–3993, Sep. 2015.
[62] D. González-Ovejero, G. Minatti, G. Chattopadhyay, and S. Maci, "Multibeam by metasurface antennas," *IEEE Trans. Antennas Propag.*, vol. 65, no. 6, pp. 2923–2930, Feb. 2017.
[63] F. Caminita, E. Martini, G. Minatti, and S. Maci, "Fast integral equation method for metasurface antennas," in *Proc. URSI Int. Symp. Electromagn. Theory (EMTS)*, Aug. 2016, pp. 480–483.
[64] F. Liu *et al.*, "Intelligent metasurfaces with continuously tunable local surface impedance for multiple reconfigurable functions," *Phys. Rev. A, Gen. Phys.*, vol. 11, no. 4, Apr. 2019, Art. no. 044024.
[65] K. Chen *et al.*, "A reconfigurable active Huygens' metalens," *Adv. Mater.*, vol. 29, no. 17, May 2017, Art. no. 1606422.
[66] M. Kim and G. V. Eleftheriades, "Guided-wave-excited binary Huygens' metasurfaces for dynamic radiated-beam shaping with independent gain and scan-angle control," *Phys. Rev. A, Gen. Phys.*, vol. 15, no. 5, May 2021, Art. no. 054037.
[67] S. Foo, "Liquid-crystal reconfigurable metasurface reflectors," in *Proc. IEEE Int. Symp. Antennas Propag. USNC/URSI Nat. Radio Sci. Meeting*, Jul. 2017, pp. 2069–2070.
[68] J. Shabanpour, S. Beyraghi, and A. Cheldavi, "Ultrafast reprogrammable multifunctional vanadium-dioxide-assisted metasurface for dynamic THz wavefront engineering," *Sci. Rep.*, vol. 10, no. 1, Dec. 2020, Art. no. 8950.
[69] A. Li, Z. Luo, H. Wakatsuchi, S. Kim, and D. F. Sievenpiper, "Nonlinear, active, and tunable metasurfaces for advanced electromagnetics applications," *IEEE Access*, vol. 5, pp. 27439–27452, 2017.
[70] E. Martini *et al.*, "Reconfigurable antenna based on liquid crystals for continuous beam scanning with a single control," in *Proc. IEEE Int. Symp. Antennas Propag. USNC-URSI Radio Sci. Meeting*, Jul. 2019, pp. 449–450.
[71] S. C. Pavone, E. Martini, F. Caminita, M. Albani, and S. Maci, "Surface wave dispersion for a tunable grounded liquid crystal substrate without and with metasurface on top," *IEEE Trans. Antennas Propag.*, vol. 65, no. 7, pp. 3540–3548, Jul. 2017.
[72] C. D. Giovampaola, F. Caminita, G. Labate, E. Martini, and S. Maci, "Experimental verification of a 5G active metasurface antenna with beam steering capabilities," in *Proc. 15th Eur. Conf. Antennas Propag. (EuCAP)*, 2021.
[73] D. González-Ovejero *et al.*, "Basic properties of checkerboard metasurfaces," *IEEE Antennas Wireless Propag. Lett.*, vol. 14, pp. 406–409, 2014.
[74] H. Krraoui *et al.*, "Characterization of optically-reconfigurable metasurfaces by a free space microwave bistatic technique," *Appl. Sci.*, vol. 10, no. 12, p. 4353, Jun. 2020.

Open Access funding provided by 'University of Siena' within the CRUI CARE Agreement